

MIT Open Access Articles

The neuropeptide NMU amplifies ILC2-driven allergic lung inflammation

The MIT Faculty has made this article openly available. **Please share** how this access benefits you. Your story matters.

Citation: Wallrapp, Antonia et al. "The Neuropeptide NMU Amplifies ILC2-Driven Allergic Lung Inflammation." *Nature* 549, 7672 (September 2017): 351–356 © 2017 Macmillan Publishers Limited, part of Springer Nature

As Published: <http://dx.doi.org/10.1038/NATURE24029>

Publisher: Nature Publishing Group

Persistent URL: <http://hdl.handle.net/1721.1/116796>

Version: Author's final manuscript: final author's manuscript post peer review, without publisher's formatting or copy editing

Terms of Use: Article is made available in accordance with the publisher's policy and may be subject to US copyright law. Please refer to the publisher's site for terms of use.





Published in final edited form as:

Nature. 2017 September 21; 549(7672): 351–356. doi:10.1038/nature24029.

The neuropeptide NMU amplifies ILC2-driven allergic lung inflammation

Antonia Wallrapp^{1,*}, Samantha J. Riesenfeld^{2,*}, Patrick R. Burkett^{1,3,*}, Raja-Elie E. Abdunour³, Jackson Nyman², Danielle Dionne², Matan Hofree², Michael S. Cuoco², Christopher Rodman², Daneyal Farouq², Brian J. Haas², Timothy L. Tickle², John J. Trombetta², Pankaj Baral⁴, Christoph S. N. Klose⁵, Tanel Mahlaköiv⁵, David Artis⁵, Orit Rozenblatt-Rosen², Isaac M. Chiur⁴, Bruce D. Levy³, Monika S. Kowalczyk², Aviv Regev^{2,6}, and Vijay K. Kuchroo^{1,2}

¹Evergrande Center for Immunologic Diseases, Harvard Medical School and Brigham and Women's Hospital, Boston, Massachusetts, USA

²Klarman Cell Observatory, Broad Institute of MIT and Harvard, Cambridge, Massachusetts, USA

³Division of Pulmonary and Critical Care Medicine, Department of Medicine, Brigham and Women's Hospital, Boston, Massachusetts, USA

⁴Department of Microbiology and Immunobiology, Division of Immunology, Harvard Medical School, Boston, Massachusetts, USA

⁵Jill Roberts Institute for Research in Inflammatory Bowel Disease, Joan and Sanford I. Weill Department of Medicine, Department of Microbiology and Immunology, Weill Cornell Medical College, Cornell University, New York, New York, USA

⁶Howard Hughes Medical Institute and David H. Koch Institute for Integrative Cancer Research, Department of Biology, MIT, Cambridge, Massachusetts, USA

Reprints and permissions information is available at www.nature.com/reprints.

Correspondence and requests for materials should be addressed to P.R.B. (pburkett@rics.bwh.harvard.edu), M.S.K. (monika@broadinstitute.org), A.R. (aregev@broadinstitute.org) or V.K.K. (vkuchroo@evergrande.hms.harvard.edu).

*These authors contributed equally to this work.

Online Content Methods, along with any additional Extended Data display items and Source Data, are available in the online version of the paper; references unique to these sections appear only in the online paper.

Supplementary Information is available in the online version of the paper.

Author Contributions P.R.B., A.R. and V.K.K. co-conceived the study. P.R.B., A.W., S.J.R., M.S.K., V.K.K. and A.R. designed the experiments and interpreted results. A.W. and P.R.B. performed and analysed the functional biological experiments, including preparation of cells for scRNA-seq, except immunofluorescence microscopy. S.J.R. designed and performed the computational analysis, with assistance from M.H., M.S.C., B.J.H. and T.L.T. M.S.K. directed scRNA-seq efforts, in conjunction with O.R. M.S.K., J.N., D.D., C.R., D.F. and J.J.T. performed scRNA-seq. R.A.E. and B.D.L. assisted with measuring airway resistance. C.S.N.K., T.M. and D.A. performed and analysed immunofluorescence staining of the lung. P.B. and I.C. assisted with analysis of neurons. The manuscript was written by P.R.B., S.J.R. and A.W., and was edited by A.R. and V.K.K., with input from all the authors.

Author Information The authors declare competing financial interests: details are available in the online version of the paper. Readers are welcome to comment on the online version of the paper.

Publisher's note: Springer Nature remains neutral with regard to jurisdictional claims in published maps and institutional affiliations.

Code availability Code will be made available upon request.

Data availability The data discussed in this publication have been deposited in the NCBI Gene Expression Omnibus and are accessible through GEO Series accession number GSE102299. Processed scRNA-seq data can be visualized and downloaded at https://portals.broadinstitute.org/single_cell/study/lung-ilcsunder-alarmin-and-neuropeptide-activation.

Abstract

Type 2 innate lymphoid cells (ILC2s) both contribute to mucosal homeostasis and initiate pathologic inflammation in allergic asthma. However, the signals that direct ILC2s to promote homeostasis versus inflammation are unclear. To identify such molecular cues, we profiled mouse lung-resident ILCs using single-cell RNA sequencing at steady state and after *in vivo* stimulation with the alarmin cytokines IL-25 and IL-33. ILC2s were transcriptionally heterogeneous after activation, with subpopulations distinguished by expression of proliferative, homeostatic and effector genes. The neuropeptide receptor *Nmur1* was preferentially expressed by ILC2s at steady state and after IL-25 stimulation. Neuromedin U (NMU), the ligand of NMUR1, activated ILC2s *in vitro*, and *in vivo* co-administration of NMU with IL-25 strongly amplified allergic inflammation. Loss of NMU–NMUR1 signalling reduced ILC2 frequency and effector function, and altered transcriptional programs following allergen challenge *in vivo*. Thus, NMUR1 signalling promotes inflammatory ILC2 responses, highlighting the importance of neuro-immune crosstalk in allergic inflammation at mucosal surfaces.

Given the increased prevalence of allergy and asthma, identifying the molecular pathways that modulate the response of type 2 innate lymphoid cells (ILC2s) to alarmins is an important area of inquiry. Damaged or stressed epithelial cells produce alarmin cytokines, such as IL-25 and IL-33, which activate ILC2s^{1–5}. Activated ILC2s initiate allergic tissue inflammation at mucosal surfaces, in part by rapidly producing effector cytokines, such as IL-5 and IL-13^{6–8}. ILC2s also maintain tissue homeostasis by promoting epithelial cell proliferation, survival, and barrier integrity⁹. However, the factors that balance homeostatic and inflammatory ILC2 responses are unknown, as is whether distinct ILC2 subsets mediate these effects.

It is challenging to distinguish homeostatic from pro-inflammatory ILC2s, since there are few known markers of these functional states. Single-cell genomics, especially single-cell RNA-sequencing (scRNA-seq)^{10,11}, can identify such diversity, both when changes in cell states are continuous across a population¹² and when there are discrete subpopulations of varying sizes, including in intestinal ILCs^{13–15}.

Alarmins induce heterogeneity in ILC2s

To define the transcriptional landscape of lung-resident ILCs, we collected 24,187 high-quality, droplet-based scRNA-seq profiles of ILCs (IL-7Ra⁺CD90⁺ and lacking lineage markers) at steady state and after *in vivo* activation by IL-25 or IL-33 (Fig. 1a, Extended Data Fig. 1a–c). We scored cells based on expression of ILC subset-specific signature genes (after condition-specific normalization, Methods), and classified cells as ILC1, ILC2, ILC3, ‘mixed’, or ‘none’ if no score was sufficiently high (Extended Data Fig. 1d–f, Methods). Mixed profile ILCs could either represent a transient or plastic transcriptional state or cell doublets. Expression of key signature genes (for example, *Tbx21*, *Il1rl1*, *Rorc*) supported our cell classification (Extended Data Fig. 1g). ILC2s composed greater than 94% of cells in all conditions; IL-33 increased their proportion further, whereas IL-25 increased the proportion of ILC3s (Extended Data Fig. 1e) (multinomial logistic; IL-33, $P < 2.2 \times 10^{-16}$; IL-25, $P < 8.4 \times 10^{-8}$).

Alarmin treatment induced unique gene expression programs, as suggested by the relationship between the expression profiles of cells from different treatment conditions, independent of experimental batch (Fig. 1a, Extended Data Fig. 1h). IL-25 and IL-33 both upregulated genes associated with ILC2 activation, including *Il5*, *Klrg1*, and *Arg1*, while other genes, such as *Areg*, were preferentially induced by one alarmin but not the other (Extended Data Fig. 1i)^{2,16}.

We partitioned transcriptionally distinct ILCs into 11 clusters (Fig. 1b). All clusters exhibited high expression of key marker genes of ILCs, while markers of other cell types were minimally expressed, except for CD3 genes (Extended Data Fig. 1j; *Cd3d*), which have previously been observed at the mRNA level in ILCs^{17,18}. ILC1s, ILC2s and ILC3s largely partitioned into distinct clusters. ILC1s composed approximately 50% of cluster 1 (392 cells; 56% of ILC1s), ILC3s and mixed ILCs each made up around 25% of cluster 2 (926 cells; 64% of ILC3s), and the remaining clusters (22,869 cells) were predominantly composed of ILC2s, particularly clusters 3–5 and 8–11 (Fig. 1c, Extended Data Fig. 1k). Cluster assignment is strongly associated with treatment (χ^2 test, $P < 2.2 \times 10^{-16}$): most cells in clusters 7 and 9–11 are IL-33-activated ILCs, while cells in clusters 5 and 8 are primarily IL-25-activated ILCs, and control ILC2s comprise approximately 90% of clusters 3 and 4 (Fig. 1d, Extended Data Fig. 1l).

Alarmin-activated ILCs express 1.5–2.5-fold more genes than do resting ILCs, partly owing to proliferation, particularly among IL-33-activated ILC2s (Extended Data Fig. 1c). Clusters 7 and 11, enriched with such cells, scored highly for a proliferative gene signature (t -test, $P < 2.2 \times 10^{-16}$) (Fig. 1e)^{19,20}. Consistent with this, IL-33 induced more robust proliferation of ILCs *in vitro* than did IL-25 (Extended Data Fig. 2).

To uncover novel molecular cues that regulate ILC responses, we identified genes that were differentially expressed across clusters by fitting gene counts to mixtures of generalized linear models that account for variation in both dropout rates and proliferation (Methods, Supplementary Table 1). Highly differentially expressed genes include both those with known and novel roles in ILC biology (Fig. 1f). Among known genes, *Arg1*, *Il13* and *Klrg1* are highly expressed in clusters where alarmin-activated ILC2s are predominant. Other genes discriminate between cells activated by a single alarmin. For example, clusters 5 and 8 both consist predominantly of IL-25-activated ILC2s, yet *Ms4a4b* is expressed only in cluster 8. Similarly, *Ctla4* was induced only in certain clusters of IL-25- or IL-33-activated cells (Fig. 1f).

We validated the expression patterns at the protein level for a number of genes using flow cytometry (Extended Data Fig. 1m). As predicted, KLRG1, gp49 (*Lilrb4a*), and Batf were upregulated after activation by IL-25 and IL-33. Expression of semaphorin 4a (*Sema4a*) was reduced in IL-33-activated ILCs, mirroring the lower expression in IL-33-dominant scRNA-seq clusters. Finally, consistent with the scRNA-seq data, only a subset of ILCs upregulated CTLA4 or MHC class II after alarmin activation. These results suggest that distinct functional states exist within defined ILC subsets, and that IL-33 and IL-25 differentially regulate these states.

Studies in other systems have shown that analysis of large cell numbers, even at shallow coverage, can readily identify markers of transcriptional states^{14,21}. However, the number of distinct transcripts per cell in droplet-based scRNA-seq may be lower than in full-length protocols^{22,23}. To explore the possible impact of these differences, we complemented our droplet-based survey with an analysis using a plate-based full-length protocol²³.

We analysed 606 high-quality full-length scRNA-seq profiles of ILCs from phosphate-buffered saline (PBS)-, IL-25-, or IL-33-treated mice (Fig. 2a, Extended Data Fig. 3a). Most cells were classified as ILC2s, consistent with our droplet-based atlas (Extended Data Fig. 3b–e). The two datasets were highly concordant in terms of the similarity of expression profiles (Extended Data Fig. 4a), clustering (Fig. 1a, b versus Fig. 2a, b), and top genes identified by principle component analysis (PCA) or differential expression analysis (for example, *Lpcat2*, *Anxa2*, *Lgals3bp*, *Ms4a4b*) (Fisher's exact test, $P < 3.74 \times 10^{-80}$, for PCA genes) (Figs 1f, 2c).

Of the differentially expressed genes in plate-based scRNA-seq, *Nmur1* (also known as Gpr66 and FM-3) was highly expressed in ILC2s at steady state and after IL-25 stimulation, but was downregulated by IL-33 (Fig. 2c), and yet was essentially absent in the initial droplet-based scRNA-seq analysis (Extended Data Fig. 4a). Alignment of bulk, full-length RNA-seq indicated that the *Nmur1* transcript extends to a different 3' end in lung ILCs than is annotated in the reference transcriptome (Extended Data Fig. 4b). Upon correcting the *Nmur1* annotation, *Nmur1* was recovered in the droplet-based data (Extended Data Fig. 4c). By contrast, *Rapgef4*, another of the few differentially expressed genes absent in the droplet-based data, has an annotated 3' end consistent with the bulk RNA-seq, indicating that technical issues other than transcriptome annotation also contribute to discrepancies (Extended Data Fig. 4d). Overall, however, both droplet and plate data supported the same global trends, including the differential expression of *Nmur1*.

ILC2-specific expression of NMUR1

NMUR1 is a receptor for the neuropeptide NMU, and NMU–NMUR1 signalling modulates inflammatory responses²⁴, although the role of this pathway in ILCs was unknown. We found that *Nmur1* expression was largely specific to ILCs, compared to other lung-resident cell populations. It was highly expressed in ST2⁺ ILCs both at steady state and after induction of airway inflammation with house dust mite (HDM) extract (Fig. 2d). In either setting, the only non-ILC population with detectable *Nmur1* expression was CD4⁺ T cells, which expressed very low levels both after HDM-challenge *in vivo*, as well as after T helper 2 (T_H2) differentiation *in vitro* (Fig. 2d, Extended Data Fig. 5a). *Nmur2*, the other known receptor for NMU, was not detectably expressed in lung-resident cells, including ILCs, but was expressed in the central nervous system, as previously reported (Extended Data Fig. 5b)^{25–27}.

We assessed NMUR1 protein expression by flow cytometry of cells from heterozygous *Nmur1-LacZ* reporter mice. Approximately 40% of ST2⁺ ILCs expressed NMUR1 (Fig. 2e, Extended Data Fig. 5c). Only ILC2s had notable specific staining, although several myeloid cell types demonstrated non-specific staining independent of the reporter allele (Extended

Data Fig. 5d). Treatment *in vivo* with IL-25 did not alter the frequency of NMUR1⁺ ILCs, whereas IL-33 markedly reduced their frequency (Fig. 2f). Regardless of alarmin treatment, NMUR1 was predominantly expressed by ST2⁺ ILCs and did not correlate with expression of IL-17RB, the receptor for IL-25 (Extended Data Fig. 5e).

ILCs express several neuropeptide receptors in addition to NMUR1^{28,29}, raising the possibility that neurons communicate directly to ILCs. Immunofluorescence microscopy showed that around 70% of CD3⁺KLRG1⁺ cells are within 10 µm of SNAP-25⁺ nerve fibres (Extended Data Fig. 6a). The nodose/jugular ganglion and thoracic dorsal root ganglia (DRG) both contain sensory afferent neurons innervating the lung^{28,30}, and neurons in the DRG, although not in the nodose/jugular ganglion, express *Nmu* (Extended Data Fig. 6b). Additionally, IL-13 induced upregulation of *Nmu* in cultured DRG neurons, suggesting ILCs may also communicate with neurons (Extended Data Fig. 6c).

NMU amplifies IL-25-driven inflammation

We next investigated whether NMU affected ILC production of type 2 cytokines *in vitro*. While NMU did not affect cytokine expression by T_H2 cells (Extended Data Fig. 7a) and only mildly upregulated *Il5* and *Il13* in cultured ILC2s, NMU markedly increased their mRNA and protein expression when combined with IL-25, suggesting that NMU modulates ILC2 responses to alarmins (Fig. 3a, b, Extended Data Fig. 7b). The combination of IL-33 and NMU also increased IL-5 and IL-13 expression, but to a lesser extent than IL-25 combined with NMU (Extended Data Fig. 7c).

The synergy between IL-25 and NMU was even more notable *in vivo*. NMU alone did not increase expression of *Il5* or *Il13* mRNA in lung tissue, and only trace quantities of IL-5 protein were detectable in the bronchoalveolar lavage fluid (BALF), consistent with a small increase in BALF eosinophils (Extended Data Fig. 7d–h). IL-25 modestly induced expression of IL-5 and IL-13 in the lung and BALF, while the combination of IL-25 and NMU strongly increased their expression (Fig. 3c, Extended Data Fig. 7i). Moreover, IL-25 combined with NMU increased lung and BALF eosinophilia, and markedly enhanced histopathologic evidence of inflammation (Fig. 3d, e, Extended Data Fig. 7j). Finally, IL-25 combined with NMU induced significant airway hyper-reactivity (Fig. 3f). In summary, NMU converted a non-pathologic dose of IL-25 into a pathologic one.

To understand the role of endogenous NMU in ILC function, we analysed ILCs in NMU-deficient (*Nmu*-knockout) mice. At steady state, both the overall frequency of ILCs and ILC expression of KLRG1, ST2, IL-5, and IL-13 were unchanged in *Nmu*-knockout versus wild-type mice (Extended Data Fig. 8a–c). After challenge with HDM, total cell numbers and eosinophil frequencies in BALF were similar in wild-type and *Nmu*-knockout mice (Extended Data Fig. 8d). However, the frequency of ST2⁺ ILCs after HDM challenge was reduced in *Nmu*-knockout mice, compared to wild-type mice (Fig. 3g), and a lower percentage of ILCs expressed IL-5 and IL-13 *ex vivo* (Fig. 3h). The frequency of lung-infiltrating CD4 T cells was higher in *Nmu*-knockout mice, while the frequency of T cells expressing type 2 cytokines *ex vivo* was unchanged, suggesting potential adaptive immune compensation that could explain the similar degree of BALF eosinophilia (Extended Data

Fig. 8e, f). Overall, the reduced frequency of ILC2s expressing effector cytokines after allergen challenge in *Nmu*-knockout mice indicates that NMU promotes ILC activation and effector function.

IL-25 combined with NMU expands inflammatory ILC2s

To characterize how IL-25 and NMU synergistically promote allergic inflammation, we profiled lung-resident ILCs by scRNA-seq after *in vivo* treatment with NMU alone or in combination with IL-25 (Fig. 4a, Extended Data Fig. 9a, b). NMU-treated ILCs were transcriptionally similar to control ILCs, consistent with the minimal *in vivo* impact of NMU alone (Fig. 4a), whereas the expression profiles of ILCs treated with a combination of IL-25 and NMU were distinct from those of IL-25- and NMU-treated ILCs, and comparable to those of IL-33-activated ILCs (Extended Data Fig. 9c). We analysed profiles from ILCs treated with PBS, NMU, IL-25 and IL-25 combined with NMU, partitioning them into 11 clusters (Fig. 4b). There was a significant association between cluster and treatment (χ^2 test, $P < 2.2 \times 10^{-16}$). Five clusters (6 and 8–11) consisted almost exclusively of cells activated by IL-25 or IL-25 combined with NMU (Extended Data Fig. 9d, e), suggesting that IL-25 combined with NMU expands transcriptionally distinct subsets of ILCs present at lower numbers in IL-25-treated mice.

One mechanism by which IL-25 and NMU synergized was by inducing proliferation in distinct subpopulations of ILCs. Mice treated with IL-25 combined with NMU had increased ILC frequencies and approximately twice as many Ki67⁺ ILCs as IL-25-treated mice, indicating significant proliferation (Fig. 4c, Extended Data Fig. 9f). Cells activated by IL-25 combined with NMU had bimodally distributed proliferative signature scores (Fig. 4d), as cells in IL-25 and NMU-dominated cluster 11 scoring higher than cells in other clusters (t -test, $P < 2.2 \times 10^{-16}$, Extended Data Fig. 9g).

Another mechanism by which NMU could amplify IL-25-initiated ILC responses is by upregulating IL-17RB on ILCs. Compared to IL-25 alone, IL-25 combined with NMU increased the frequency of IL-17RB⁺ ILCs by flow cytometry and upregulated the expression of *Il17rb* mRNA in the lung by quantitative real-time PCR (qPCR) (Fig. 4e, Extended Data Fig. 9h). The frequency of *Il17rb*-expressing ILCs was also increased in the scRNA-seq profiles from mice treated with IL-25 combined with NMU (Fig. 4f, logistic regression, $P < 2.73 \times 10^{-10}$). Finally, IL-17RB⁺ ILC frequency after HDM challenge was reduced in *Nmu*-knockout versus wild-type mice (Fig. 4g), suggesting that NMU potentiates ILC responsiveness to IL-25 following both allergen challenge and alarmin stimulation.

We analysed differential gene expression between IL-25 combined with NMU and other conditions, focusing on genes with a non-additive pattern of expression. One subset of such genes, including *Il1r2*, *Tnfrsf8* (CD30) and *Mt1*, was strongly upregulated specifically by IL-25 combined with NMU (Fig. 4h). A second subset, including *Zfp361l* and *Csf2*, was downregulated by IL-25 combined with NMU, even though it was upregulated after treatment with IL-25 and/or NMU alone. Finally, a few genes (for example, *Btg2* and *Fosb*) were expressed at steady state and in single-treatment conditions at similar levels, but were downregulated by IL-25 combined with NMU. We validated these expression patterns for

several representative genes by flow cytometry. Consistent with the scRNA-seq data, both CD30 and IL-1R2 were upregulated only by IL-25 combined with NMU; galectin-3 (*Lgals3*) and gp49 (*Lilrb4a*) were upregulated by either NMU or IL-25 alone and further induced by IL-25 combined with NMU; and NR4A1 expression was highest in response to IL-25 alone (Extended Data Fig. 9i).

Several of these genes have previously been linked to allergic airway inflammation in both mice and humans. Mice lacking *Tnfrsf8* and *Anxa2* have reduced airway inflammation in asthma models^{31,32}. *Tnfrsf8*, *Anxa2* and *Il1r2* are overexpressed in allergic asthmatics^{33–35}. Deletion of *Nr4a1*, which is downregulated by IL-25 combined with NMU, exacerbates airway inflammation in mice, suggesting a potential role in limiting inflammatory ILC responses³⁶.

Cluster-based analysis of differentially expressed genes further highlighted that ILCs from mice treated with IL-25 combined with NMU were transcriptionally heterogeneous (Fig. 4b, Extended Data Fig. 9j). Some genes, such as *Il13*, were highly expressed in all clusters principally composed of ILC2s treated with IL-25 combined with NMU or IL-25 (clusters 6–11), while other genes were specific to certain clusters. For example, *Ifitm3* was highly expressed in ILCs in cluster 10, whereas ILCs in cluster 7, which were also expanded by IL-25 combined with NMU, co-expressed key antigen-presentation genes, including MHC class II (for example, *H2-Ab1*) and the invariant chain (*Cd74*). IL-25 combined with NMU also increased the frequency of a population of MHC-II^{hi} ILCs as determined by flow cytometry (Extended Data Fig. 9i). Cluster 8 primarily consisted of ILCs treated with IL-25 or IL-25 combined with NMU that expressed *Klrg1*, *Il13* and *Il4*, as well as some *Il17a*, but little *Il1r1* and *Il5*, similar to previous reports of an IL-25-induced KLRG1^{hi}ST2[–] inflammatory ILC2 (iILC2) population². ILCs of cluster 8 also expressed *Nmur1*, as did cells in IL-25 predominant cluster 6, suggesting that these two subsets are preferentially NMU-responsive. Flow cytometry revealed that NMUR1 was expressed by IL-25-treated ILCs, including iILC2s (Extended Data Fig. 9k). While both IL-25 combined with NMU and IL-33 downregulated NMUR1 on ILC2s, IL-25 combined with NMU uniquely expanded the population of iILC2s, suggesting that NMU–NMUR1 signalling preferentially modulates the activation and/or expansion of certain IL-25-induced iILC2 subsets (Extended Data Fig. 9l, m).

NMUR1 promotes ILC2 activation by HDM

To further characterize the impact of NMUR1 signalling on ILCs, we challenged wild-type and *Nmur1*-knockout mice with HDM and profiled lung-resident ILCs by scRNA-seq. Analysis of 21,895 high-quality profiles largely clustered them by *in vivo* treatment, regardless of genotype or batch (Fig. 5a, Extended Data Fig. 10a, b). In *Nmur1*-knockout mice, ILC2 frequency was markedly reduced after HDM challenge compared to PBS (76% versus 91%; multinomial logistic, $P < 2.2 \times 10^{-16}$), exaggerating a trend also seen in wild-type mice (87% versus 94%, multinomial logistic, $P < 2.2 \times 10^{-16}$), which is consistent with the reduced frequency of ST2⁺ ILCs in *Nmu*-knockout mice after HDM challenge (Fig. 5b, Extended Data Fig. 10c, d). While IL-25 combined with NMU and IL-33 induced robust proliferation and increased ILC2 frequency, HDM challenge only induced a high

proliferation score in the cells of one small cluster (cluster 6, 210 cells) (Fig. 1e, Extended Data Figs 1e, 10e–h). This minimal induction of proliferation, in conjunction with an increase in ILC1s and ILC3s, may be related to the observed reduction in ILC2 frequency after HDM challenge.

Based on genes differentially expressed between HDM- and PBS-treated wild-type ILC2s, we defined an inflammatory ILC2 signature (Fig. 5c–e). ILCs from mice treated with IL-25 combined with NMU scored highly for this inflammatory signature, suggesting that it identifies inflammatory ILC2s independent of the model of airway inflammation (Fig. 5d, e). Differentially expressed genes in ILC2s from HDM-treated mice significantly overlapped with those in ILCs from mice treated with IL-25 combined with NMU (Fisher's exact test, $P < 1.64 \times 10^{-25}$). Finally, *Nmur1*-knockout ILC2s had a lower average inflammatory score than wild-type ILC2s after HDM challenge (*t*-test, $P < 4.9 \times 10^{-15}$), consistent with NMU–NMUR1 signalling promoting ILC2 responses *in vivo* (Fig. 5e).

Discussion

We used massively parallel droplet-based scRNA-seq to establish the transcriptional landscape of lung-resident ILCs under homeostatic and inflammatory conditions, and identified NMUR1 as a modulator of alarmin- and allergen-driven ILC2 responses. *Nmu*-knockout mice were previously reported to develop attenuated airway inflammation after allergic sensitization²⁴, but the underlying mechanism was unclear. NMU expression in bronchial brushing samples from asthmatic patients correlates with disease severity, which our data suggests could be related to the effect of NMU on ILC function³⁷. Functional analysis and scRNA-seq-based approaches both demonstrate that, in the absence of NMU–NMUR1 signalling, ILC2s are decreased in frequency and have impaired effector function after allergen challenge. Although the inflammatory signature score of allergen-challenged NMUR1-deficient ILC2s is significantly decreased compared to allergen-challenged wild-type ILC2s, it is still increased compared to PBS-treated controls, suggesting that other factors, in addition to NMU, contribute to ILC activation in this context.

Our findings raise the question of whether NMU potentiates airway inflammation when high levels of alarmins, such as IL-25, are present, as is the case in steroid-naïve T_H2-high asthma or post-viral asthma exacerbations^{1,38}. While airway epithelial cells upregulate IL-25 in response to stress, chemosensory cells, which are found in both the intestine and trachea, constitutively produce IL-25 and modulate mucosal immune responses^{39–43}. Our observation that NMU is expressed by neurons from thoracic DRG suggests that the coordinated action of neurons and chemosensory cells could promote tissue-based, ILC-dependent type 2 immune responses. Given the importance of smooth muscle contraction in the clinical manifestations of allergic diseases, it is intriguing that NMU can induce both smooth muscle contraction⁴⁴ and ILC2-driven inflammation. Neuronal activation following inhalation of noxious substances or allergens could potentially trigger both processes, simultaneously promoting physical expulsion and allergic immunity to the provoking stimulus. Taken together, our findings demonstrate a novel neuro-immune pathway that exacerbates mucosal allergic inflammation *in vivo*.

METHODS

Mice and *in vivo* ILC activation

C57Bl/6J mice were purchased from the Jackson Laboratory. *Nmur1*-LacZ reporter mice with a LacZ cassette knocked into the *Nmur1* locus were rederived from *Nmur1^{tm1.1(KOMP)Vlcg}* sperm obtained from the trans-NIH Knockout Mouse Project (KOMP) Repository. NMU-deficient mice (*Nmu*-knockout) were rederived from B6.129S2-NMU < tm1Mko > embryos from the RIKEN BioResource Center. For experiments with *Nmur1*-LacZ (*Nmur1*-knockout) and *Nmu*-knockout mice, littermates that were either homozygous or heterozygous for the wild-type allele were used as controls. Mice were housed under specific-pathogen-free conditions. For experiments, mice were matched for sex and age, and most mice were 6–10 weeks old. Where indicated, mice were anaesthetized with isoflurane and treated intranasally with the indicated stimuli (500 ng IL-25, 500 ng IL-33, or 20 µg neuromedin U) daily for three consecutive days. The total administered volume was 20 µl for all conditions. Mice were randomly assigned to treatment groups after matching for sex and age. Airway inflammation was also induced with house dust mite (HDM) extract (Greer Laboratories). Mice were treated intranasally with 10 µg HDM on day 0, 7, 8 and 9, before being euthanized on day 10. No power analysis was performed. The investigators were not blinded to allocation during experiments and outcome assessment except for the severity score of airway inflammation. All experiments were conducted in accordance with animal protocols approved by the Harvard Medical Area Standing Committee on Animals or BWH IACUC.

Flow cytometry

For flow cytometric analysis CD3e (clone: 145-2C11), CD4 (clone: RM4-5), CD8a (clone: 53-6.7), CD11b (clone: M1/70), CD11c (clone: N418), CD19 (clone: 6D5), CD30 (Tnfrsf8; clone: mCD30.1), CD45 (clone: 30-F11), CD47 (clone: miap301), CD48 (clone: HM48-1), CD81 (clone: Eat-2), CD90.2 (clone: 30-H12), CD127 (clone: A7R34), CD152 (CTLA-4; clone: UC10-4B9), I-A/I-E (clone: M5/114.15.2), IL-5 (clone: TRFK5), KLRG1 (clone: 2F1/KLRG1), NK1.1 (clone: PK136), Sema4A (clone: 5E3/SEMA4A), ST2 (clone: DIH9), TCRβ (clone: H57-597) and TCRγδ (clone: GL3) were purchased from BioLegend. 7AAD was obtained from BD Pharmingen, CD121b (IL1r2; clone: 4E2), Batf (clone: S39-1060) and Siglec-F (clone: E50-2440) from BD Biosciences and CD85k (gp49; clone: H1.1), Fixable Viability Dye eFluor 506, galectin-3 (Lgals3; clone: eBioM3/38), IL-13 (clone: eBio13A), IL17RB (IL-25R; clone: Munc33), Ki-67 (clone: SolA15) and Nur77 (Nr4a1) (clone: 12.14) from eBioscience. Cells were stained on ice with antibodies for surface molecules and the live/dead marker 7AAD and analysed on a LSRFortessa (BD Biosciences). Intracellular cytokine staining was performed after incubation for 5 h with 1 µM ionomycin (Sigma-Aldrich), 50 ng ml⁻¹ phorbol 12-myristate 13-acetate (Sigma-Aldrich) and GolgiStop (BD Biosciences). Cells were then fixed and stained using the BD Cytofix/Cytoperm buffer set (BD Biosciences) per manufacturer's instructions. Proliferation was assessed by Ki-67 staining after cell fixation and permeabilization using the Foxp3/Transcription Factor Staining Buffer Set (eBioscience). Different cell types were identified by the following gating strategies: ST2⁺ ILCs (7AAD⁻ CD45⁺CD4⁻Lineage⁻CD90.2⁺CD127⁺ST2⁺), T cells (7AAD⁻CD45⁺CD4⁺), B cells

(7AAD⁻CD45⁺CD19⁺), eosinophils (7AAD⁻CD45⁺CD11b⁺CD11c^{low}Siglec-F⁺SSC^{high}), neutrophils (7AAD⁻CD45⁺CD11c^{low}CD11b⁺Ly6G⁺CD11b⁺), alveolar macrophages (7AAD⁻CD45⁺CD11c^{high}CD11b^{intermediate}) and CD45⁻ cells (7AAD⁻CD45⁻).

Lung analysis

Mice were euthanized and perfused with cold PBS. Where indicated, after perfusion, broncho-alveolar lavage (BAL) was obtained by injecting 1.5 ml cold PBS into the lungs via a secured tracheal cannula. BALF was centrifuged, and the supernatant was used for analysing cytokine levels and the cell pellet was resuspended, counted, and used for flow cytometry. Following BAL, lung lobes were dissected. The post-caval lobe was fixed in buffered formalin for histological analysis. Single cell suspensions of the remaining lung parenchymal tissue were prepared with the GentleMACS lung dissociation kit (Miltenyi Biotec) according to the manufacturer's instructions. Where indicated, cells were diluted in 10% Trypan Blue and viable cells counted using a hemocytometer.

Fluorescence-activated cell sorting of innate lymphoid cells

After dissociation, single cell suspensions were incubated with CD90.2 MicroBeads (Miltenyi Biotec) on ice and enriched for CD90.2⁺ cells by magnetic separation using LS columns according to the manufacturer's protocol. CD90.2⁺ lung cells were then stained on ice with antibodies for sorting. ILCs were defined as 7AAD⁻CD45⁺CD90.2⁺CD127⁺Lineage⁻ (lineage markers: CD11b, CD11c, CD19, NK1.1, CD3e, CD4, CD8a, TCR β , TCR $\gamma\delta$) cells and sorted on a BD FACS Aria (BD Biosciences).

RNA-seq

For population (bulk) RNA-seq, sorted ILCs were lysed with RLT Plus buffer and RNA was extracted using the RNeasy Plus Mini Kit (Qiagen). Full-length RNA-seq libraries were prepared as previously described⁴⁵ and paired-end sequenced (75 bp \times 2) with a 150 cycle Nextseq 500 high output V2 kit.

For droplet-based 3' end massively parallel single-cell RNA sequencing (scRNA-seq), sorted ILCs were encapsulated into droplets, and libraries were prepared using Chromium Single Cell 3' Reagent Kits v2 according to manufacturer's protocol (10 \times Genomics). The generated scRNA-seq libraries were sequenced using a 75 cycle Nextseq 500 high output V2 kit.

For full-length scRNA-Seq, single ILCs were sorted into 96-well plates containing 5 μ l TCL Buffer (QIAGEN) with 1% 2-mercaptoethanol, centrifuged and frozen at -80 °C. SMART-Seq2 protocol was carried out as previously described²³ with minor modifications in the reverse transcription step (M.S.K. and A.R., in preparation). cDNA was amplified with 22 cycles and tagged with one-eighth of the standard Illumina NexteraXT reaction volume. Single-cell libraries were pooled and paired-end sequenced (38 bp \times 2) with a 75 cycle Nextseq 500 high output v2 kit.

All RNA-seq data represent pooled data from at least two distinct biological replicates.

ILC *in vitro* culture

For *in vitro* experiments 5,000 ILCs per well were cultured in a 96-well round bottom plate with 20 ng ml⁻¹ IL-7 (R&D Systems), 200 ng ml⁻¹ IL-25 (R&D Systems) or 20 ng ml⁻¹, 2 ng ml⁻¹ or 0.2 ng ml⁻¹ IL-33 (BioLegend) with or without 1 µg ml⁻¹ neuromedin U (US Biological). In some cases purified CD90.2⁺ lung cells were first labelled with CellTrace Violet (Thermo Fisher Scientific), then sorted as described above, and cultured for three days under the indicated conditions.

Histology

Following paraffin embedding, sections of the formalin-fixed lung lobe were stained by H&E staining. Tissue sections were scored by a histopathologist in a blinded manner for severity of lung inflammation according to the following scoring system: 0, normal; 1, very mild; 2, mild; 3, moderate; 4, severe.

Methacholine challenge

Airway hyper-responsiveness was determined as previously described²⁸ using a flexiVent rodent ventilator (SciReq).

LacZ reporter assay

The *Nmur1* null allele contains a LacZ reporter cassette. Single-cell suspensions of lung cells from *Nmur1*-LacZ^{+/-} mice were stained with the FluoReporter lacZ flow cytometry kit (Thermo Fisher Scientific) according to the manufacturer's protocol. Immediately after fluorescein di-V-galactoside (FDG) loading was stopped with 1.8 ml ice-cold medium, cells were stained with 7AAD and antibodies against surface markers and analysed by flow cytometry.

Quantitative real-time PCR

RNA was isolated using RNeasy Plus Mini Kit (Qiagen) and reverse transcribed to cDNA with iScript cDNA Synthesis Kit (Bio-Rad). Gene expression was analysed by quantitative real-time PCR on a ViiA7 System (Thermo Fisher Scientific) using TaqMan Fast Advanced Master Mix (Thermo Fisher Scientific) with the following primer/probe sets: *Il5* (Mm00439646_m1), *Il13* (Mm00434204_m1), *Il17rb* (Mm00444709_m1), *Nmur1* (Mm04207994_m1), *Nmur2* (Mm00600704_m1), *Nmu* (Mm00479868_m1) and *Actb* (Applied Biosystems). Expression values were calculated relative to *Actb* detected in the same sample by duplex qPCR.

Cytokine quantification

Cytokine concentrations in BAL fluid, lung and supernatant of *in vitro* ILC cultures were analysed by the LegendPlex Mouse Th Cytokine Panel (13-plex) (BioLegend) according to the manufacturer's instructions and analysed on a FACS Calibur (BD Biosciences).

T cell *in vitro* culture

CD4⁺ T cells were isolated as described previously⁴⁶ and sorted for naive T cells (CD4⁺CD62L⁺CD44^{low}) on a FACS Aria. Naive T cells were cultured in the presence of

plate-bound anti-CD3 ($1 \mu\text{g ml}^{-1}$; Bio X Cell) and anti-CD28 ($1 \mu\text{g ml}^{-1}$; Bio X Cell) antibodies. T_H2 cells were generated by addition of 20 ng ml^{-1} IL-4 (Miltenyi Biotec) and 20 ng ml^{-1} anti-IFN γ (Bio X Cell) antibody. On day 3 of *in vitro* differentiation, PBS, 200 ng ml^{-1} IL-33 (BioLegend) or 100 ng ml^{-1} IL-25 (R&D Systems) were added to the T cell culture either with or without $1 \mu\text{g ml}^{-1}$ NMU (US Biological). After 2 additional days, RNA was isolated.

Nodose/jugular and dorsal root ganglion isolation and cultures

Nodose/jugular ganglion and dorsal root ganglia (DRG) were dissected from mice and dissociated in 1 mg ml^{-1} collagenase A with 3 mg ml^{-1} dispase II (Roche Applied Sciences) in HEPES buffered saline (Sigma) for 60 min at 37°C . For some experiments, cells were then lysed in RLT Plus buffer and RNA was isolated using the RNeasy Plus Mini Kit (Qiagen). For the purposes of cell culture, the DRG cell suspension was then triturated with glass pasteur pipettes of decreasing size, followed by centrifugation over a 12% BSA (Sigma) gradient. After centrifugation, the top layer of neuronal debris was discarded and the DRG pellet was resuspended in neurobasal (NB) media containing B-27 and penicillin/streptomycin (Life Technologies). DRGs were then plated on laminin-coated 96-well culture dishes in NB media with B27, 50 ng ml^{-1} nerve growth factor (NGF) and penicillin/streptomycin. The next day the cells were washed with PBS before addition of fresh NB media containing B-27, NGF and penicillin/streptomycin. DRG cultures were stimulated with 200 ng ml^{-1} IL-13 for 30 min, at which time RNA was isolated for qPCR analyses.

Immunofluorescence microscopy

Mice were perfused with 37°C PBS via the heart. The lungs were extracted and inflated via the trachea with 4% low melting agarose (16520-100; Invitrogen) and fixed in 4% PFA on ice for 1 h. The lungs were embedded in agarose for vibratome cutting (Leica). $100\text{-}\mu\text{m}$ lung slices were blocked first with the mouse on mouse blocking reagent (Vector Laboratories) and subsequently with 5% goat and donkey serum (Jackson ImmunoResearch) in PBS/0.1% Triton X-100. Tissue was stained for rat anti-CD3e (17A2; BioLegend), hamster anti-KLRG1 (2F1; eBioscience) and mouse anti-SNAP-25 (SMI81; BioLegend) overnight at 4°C shaking. After washing in PBS, tissues were incubated at room temperature for 1 h in PBS/0.1% Triton X-100 containing goat anti-rat-AF555, goat anti-hamster-AF647, or goat anti-mouse IgG1-AF488 (all ThermoFisher Scientific) and then washed again. Images were acquired with an inverted Nikon Eclipse Ti microscope (Nikon). Z-stacks were acquired and converted into all-in-focus images using the Extended Depth of Focus (EDF) plug-in (NIS-Elements). Distances of KLRG1 $^{+}$ CD3e $^{-}$ cells to the closest SNAP-25 $^{+}$ nerve fibre were measured using the NIS-Elements software.

Statistical analysis of functional data

No data were excluded from analysis. Prism 7 (GraphPad Software) was used to perform two-tailed *t*-test and ordinary one-way or two-way ANOVA with Tukey's multiple comparisons test on datasets for which statistical significance is indicated (except the RNA-sequencing data). All figures of functional data show mean \pm s.e.m.

P values in transcriptomic analysis

For certain types of numeric computations, the smallest *P* value that R can report is $<2.2 \times 10^{-16}$.

Analysis of droplet-based scRNA-seq samples: initial QC

Gene counts were obtained by aligning reads to the mm10 genome using CellRanger software (v1.2 for data from alarmin-treated and NMU-treated mice, v1.3 for data from HDM-treated mice) (10× Genomics), with the genome re-annotated at the 3' end of *Nmur1* (see main text). To remove doublets and poor-quality cells, cells were excluded from subsequent analysis if they were outliers in their sample of origin in terms of number of genes, number of unique molecular identifiers (UMIs), and percentage of mitochondrial genes (Extended Data Fig. 1b, c). The number of UMIs per cell and number of genes expressed per cell are tightly correlated with condition (Extended Data Fig. 1c), probably due to the effect of proliferation on transcript numbers. Sample-specific cut-offs ranged from 626–2,483 genes per cell for a PBS-treated sample to 1,502–5,260 genes per cell for an IL-33 treated sample. At least 92% of cells were retained for each sample.

To further estimate and remove technical variability from the overall increased variability across replicates in group C (defined below), additional QC measures were taken (Extended Data Fig. 10a, b). UMI and gene saturation were estimated independently for each cell by subsampling a fraction of the total number of reads, with replacement, across a range of fractions (0.02 to 0.98, in 0.02 increments). For each subsample, we calculated the number of UMIs and transcripts detected. The sampling procedure was repeated ten times, and the values were used to estimate saturation limits for UMI/genes by nonlinear fitting of the following saturation function: $y = ax/(b + x) + c$. Cells were removed if they were outliers with respect to estimated saturation for either genes or UMIs. Cells were also removed if they were outliers in terms of the ratio or relative difference of the total number of UMIs with the number of unique UMIs. After all QC, 73–83% of cells in each of these samples were retained.

Parts of the subsequent analysis used the R package Seurat⁴⁷, version 1.4.0.7, which includes sparse matrix support for large datasets. To normalize gene counts while accounting for widely varying UMI counts among conditions, we used a scaling factor reflecting the expected number of UMIs in each condition. Let $w_{c,i}$ be the mean number of UMIs per cell in condition *c*, batch *i*. Seurat's LogNormalize() function was called on cells from condition *c* with the scale factor argument set to:

$$10,000 \times (w_{c,i} / \text{mean}_i(w_{\text{PBS},i}))$$

We refer to the output values as logTPX (as opposed to the default logTPM).

The 63,152 high-quality cell profiles were combined into three (non-exclusive) groups:

- Group A (24,187 cells): cells stimulated with PBS (9,623 cells), IL-25 (6,849 cells), or IL-33 (7,715 cells).

- Group B (35,542 cells): cells stimulated with PBS (9,623 cells), NMU (9,698 cells), IL-25 (6,849 cells), or IL-25 combined with NMU (9,372 cells).
- Group C (21,895 cells): cells from wild-type mice stimulated with PBS (5,393 cells) or HDM (6,280 cells), as well as *Nmur1*-knockout mice stimulated with PBS (4,191 cells) or HDM (6,031 cells).

To verify that the dataset consists of ILCs, we checked the raw counts for the expression of major markers of other immune cell groups (Extended Data Fig. 1j). For subsequent analysis, genes expressed in less than 0.1% of cells were excluded.

Analysis of droplet-based scRNA-Seq samples: signature scores

We calculated signature scores as the log of the geometric mean of the TPX values for the genes in the signature. That is, let S be a set of m genes defining a signature, and for any gene g in S and a given cell, let x_g be the expression of g in the cell in TPX. Then the signature score for that cell is calculated as

$$\log\left(\prod_g (x_g + 1)^{1/m}\right)$$

which is equivalent to the arithmetic mean of the logTPX values. Actual expression values, rather than centred or z-scored expression values were used. For several of our signatures, centreing (or z-scoring) expression values before computing signatures leads to misleading scores that are close to 0 across the whole dataset, though the corresponding gene expression is high. This is in part due to ILC2s composing the majority of the cells, and hence genes that are highly expressed by ILC2s lack sufficient variance over the dataset to be useful in a mean-centred signature.

We also did not replace these scores with a statistical comparison of them to randomized signatures selected from a null distribution (in contrast to our other studies^{20,45}). Owing to the varying proliferative responses in our cells, it is difficult to find a true null set of signatures, even after matching genes for dataset-wide mean and variance profiles. Signature scores are thus calculated in a way that is independent of the expression levels of unrelated genes in the same cell, and may be interpreted as similar to, though less noisy than, single-gene expression values.

The ILC subset signatures (ILC1, 2, 3 as used in Figs 1c, 5b, Extended Data Figs 1d–g, k, 3b–e, 10c–e) were curated based on established markers for ILC subsets (Supplementary Table 2). The proliferation signature was created by combining our previously published gene signatures^{19,20} that define G1–S and G2–M phases (Supplementary Table 2). For both ILC subset and proliferative signatures, all genes contribute positively to the signature score. For the inflammatory ILC2 signature, differentially expressed genes contribute positively to the score if they are upregulated in ILC2s from wild-type mice after HDM stimulation relative to PBS, and negatively otherwise (Supplementary Table 1).

Analysis of droplet-based scRNA-Seq samples: assigning ILC type

ILC signatures were used to assign each cell to one of the following categories: ILC1, ILC2, ILC3, 'mixed' (scoring highly for multiple ILC types), and 'none' (not scoring highly for any ILC type) (Supplementary Table 2). The frequency of mixed type ILCs (2.6%) is comparable to the expected doublet rate (3–4%). Based upon the dip in the bimodal distributions of ILC subset signature scores (Extended Data Figs 1d, 3b, 10c, d), the minimum score for assignment to a given category was set to 0.08. To be uniquely assigned to a category, the ratio of the highest score to the next highest score was required to be at least 1.25. The analysis is not sensitive to the specific ratio threshold choice of 1.25; that selection was made to balance the trade-off between the purity of the transcriptional profile of cells assigned to one of the three ILC subtype populations, and the number of cells called as mixed.

To test the strength of association between ILC type and treatment conditions, we used the R package *nnet*, version 7.3-12, to do a multinomial logistic regression on the ILC type, with replicate and condition as predictors.

Analysis of droplet-based scRNA-Seq samples: PCA, clustering, and tSNE

Variable genes were then selected using the *MeanVarPlot* function in Seurat with the *x.low.cutoff* and *y.cutoff* parameters set to 0.05 and 0.7, respectively, resulting in gene sets of size 774 (group A), 723 (group B), and 475 (group C). *PCAFast* was run on mean-centred variable genes to compute a limited number of PCs. To select the number of PCs to include for subsequent analysis, we estimated the number of eigenvalues larger than would be predicted by a null distribution for random matrices (Marchenko-Pastur law), and also assessed the decrease in marginal proportion of variance explained with larger PCs. The top 22 (groups A, B) and 13 (group C) PCs were included for subsequent analysis. We confirmed that the resulting analyses were not particularly sensitive to this exact choice.

The cells were clustered via Seurat's *FindClusters* function, which optimizes a modularity function on a *k*-nearest-neighbour graph computed from the top eigenvectors. After a range of cluster resolution parameters were tested, 0.6 (groups A and B) and 0.5 (group C) were selected because resulting clusters captured major, condition-related divisions, known subgroups, and statistically validated transcriptional distinctions of interest, while avoiding subdivisions of relatively uniform parts of the data.

To visualize the data, tSNE plots were created by calling Seurat's *RunTSNE* function, with the *dims.use* parameter set to the selected number of PCs and the *do.fast* parameter set to TRUE. A number of perplexity parameter choices were evaluated before selecting 100 (group A) and 50 (groups B and C). These perplexity settings produced tSNE plots that reflected the cluster structure found independently of tSNE, without introducing extreme artefacts. tSNE plots of cells separated by batch indicate that experimental batches appear to have a relatively minor impact on the PCA and clustering (Extended Data Figs 1h, 9b, 10b).

Analysis of droplet-based scRNA-seq samples: differential gene expression

To avoid spurious results due to cells in different conditions or clusters having vastly different amounts of mRNA, differential expression (DE) analysis accounted for the varying number of transcripts in each condition. We fit raw counts to a mixture of generalized linear models that include covariates for the log of the number of UMIs in a cell, as well as a categorical variable for the batch. Specifically, we fit a zero-inflated negative binomial model using the `zeroinfl` function⁴⁸ from the `pscl` R package⁴⁹, version 1.4.9. The zero-inflated negative binomial model combines a count component and a point mass at zero, which is relevant for scRNA-seq data where zero values are inflated owing to the technology not capturing expressed genes, particularly those with low expression¹¹. The model requires a substantial amount of data to fit, making it well suited to data generated by massively parallel methods. As an alternative to the zero-inflated negative binomial, we also performed a logistic regression by fitting a generalized linear model using the binomial family with a logit link, with the same covariates.

DE tests included the following models: (1) a cluster-based model with indicator coefficients for each cluster except the reference PBS-dominated cluster (groups A, B, and C); (2) a condition-wide model with indicator coefficients for each condition (with the PBS condition as reference) (groups A, B, and C); and (3) a direct comparison of IL-25 versus IL-33, with IL-33 as reference (group A); (4) a condition-based model with indicator coefficients for NMU and IL-25, and an additional interaction term (with the PBS condition as reference) to detect non-additive effects (group B); (5) a direct comparison between IL-25 combined with NMU and IL-25, with IL-25 as reference (group B). In group C, we restricted the DE analysis to the cells transcriptionally classified as ILC2s, in order to identify difference in these particular cells, without the analysis being driven by the change in relative proportions of ILC1s and ILC3s compared to ILC2s after HDM treatment.

Many cell-cycle genes and ribosomal protein genes are differentially expressed across conditions and clusters, particularly if there is a difference in proliferation. To detect other differentially expressed genes as well, before ranking DE results, we removed ribosomal protein genes and (in all cases except group C, where it was not needed) the genes in the proliferation signature (Supplementary Table 2).

DE tests report coefficients and associated *P* values for each variable of interest (for example, cluster or condition), separately for each model component. To rank the results for any given model, we created a list of differentially expressed candidate genes that are detected in at least 10% (15% for group C) of the cells in one of the groups in the model and have a coefficient for a term of interest with absolute value at least 0.5 (0.75 for group C) and corresponding FDR-adjusted *P* value $< 1 \times 10^{-20}$ for condition-wide DE, $< 1 \times 10^{-6}$ for cluster DE, for at least one component. We ranked these candidates by lowest *P* value and also by largest absolute value of coefficient. The top 25 genes (top 5, 5 and 3 genes for cluster models in groups A, B and C, respectively) genes according to each ranking were reported, with a minimum of 1–2 genes, if available, selected from each of the set of candidates with positive coefficients and the set with negative coefficients. These genes are reported according to the condition or cluster for which they were ranked highly, and the sign reported is ‘plus’ (‘minus’) if that condition or cluster has a higher (lower) expression

by both fraction of cells expressing and level of expression than the reference, or if these are discordant then the sign is reported as 'NA' (Supplementary Table 1).

We curated a representative selection from the highest ranked results to represent, in Fig. 1f, common, distinctive patterns across clusters in group A, and, in Fig. 4h, patterns that distinguish IL-25 combined with NMU from the other conditions in group B and highlight nonlinear interactions between NMU and IL-25. To create the inflammatory ILC2 signature (Fig. 5c–e) we used the top-ranked genes differentially expressed between HDM and PBS treatments in ILC2s only in wild-type mice, as well as those differentially expressed in HDM- and ILC2-dominated clusters (5 and 6) in this dataset. The signature genes are reported with the sign positive if the respective condition or cluster has higher expression than the reference for that model (Supplementary Table 1).

To more broadly compare differentially expressed genes between HDM and IL-25 combined with NMU datasets, we constructed one gene set for IL-25 combined with NMU by taking the top differentially expressed genes for all models and comparisons in group B in which there is a coefficient for the condition IL-25 combined with NMU or a coefficient for a group or cluster to which cells treated with IL-25 combined with NMU contribute (clusters 2, 6–11) (Supplementary Table 1). We then performed the analogous procedure in the HDM data (including clusters 1–2 and 4–7) (Supplementary Table 1). Using as the null set the 12,719 genes shared between groups B and C, we used Fisher's exact test to determine the significance of the overlap of 23 genes between the 156 genes from the IL-25 combined with NMU gene set (151 of which are in the null set) and the 85 genes from the HDM data (all of which are in the null set) ($P < 1.64 \times 10^{-25}$).

Analysis of SMART-Seq2 plate-based scRNA-seq data

Reads were aligned to mm10 using Kallisto⁵⁰ quant, version 0.42.3. The R package tximport⁵¹, version 1.2.0, was used to convert the output to gene counts and traditional TPM values. Because of the variability in read counts per cell across plates, even from the same condition, as well as in the number of genes per cell across conditions, QC was performed for each of eight plates individually in order to remove cells that were outliers or too low with respect to either measure (Extended Data Fig. 3a). Out of 752 cells, 606 cells met QC criteria (234 from control, 152 from IL-25-treated mice, and 220 from IL-33-treated mice), and the number of genes per cell in this set ranged from 1,625 to 6,375. Genes that were not expressed with $\log(\text{TPM}) > 2.5$ in at least two cells were removed from further analysis. Subsequent analysis proceeded analogously to the droplet-based RNA-seq analysis, with parameter settings that reflected both the wider dynamic range of expression and much smaller cell numbers. The minimum ILC signature score required in ILC type assignment was 0.3. Variable genes were identified by running MeanVarPlot with $x.\text{low.cutoff} = 0.1$, $y.\text{cutoff} = 1.5$, and $x.\text{high.cutoff} = 10$, resulting in a set of 519 genes. PCA was performed on the mean-centred expression of variable genes, with 9 PCs chosen for the subsequent clustering analysis (resolution parameter 0.6). RuntSNE was called with the default perplexity value of 30.

The DE analysis for plate-based data followed the structure of the droplet-based analysis but used only logistic regression, with both a condition-based model and a cluster-based model.

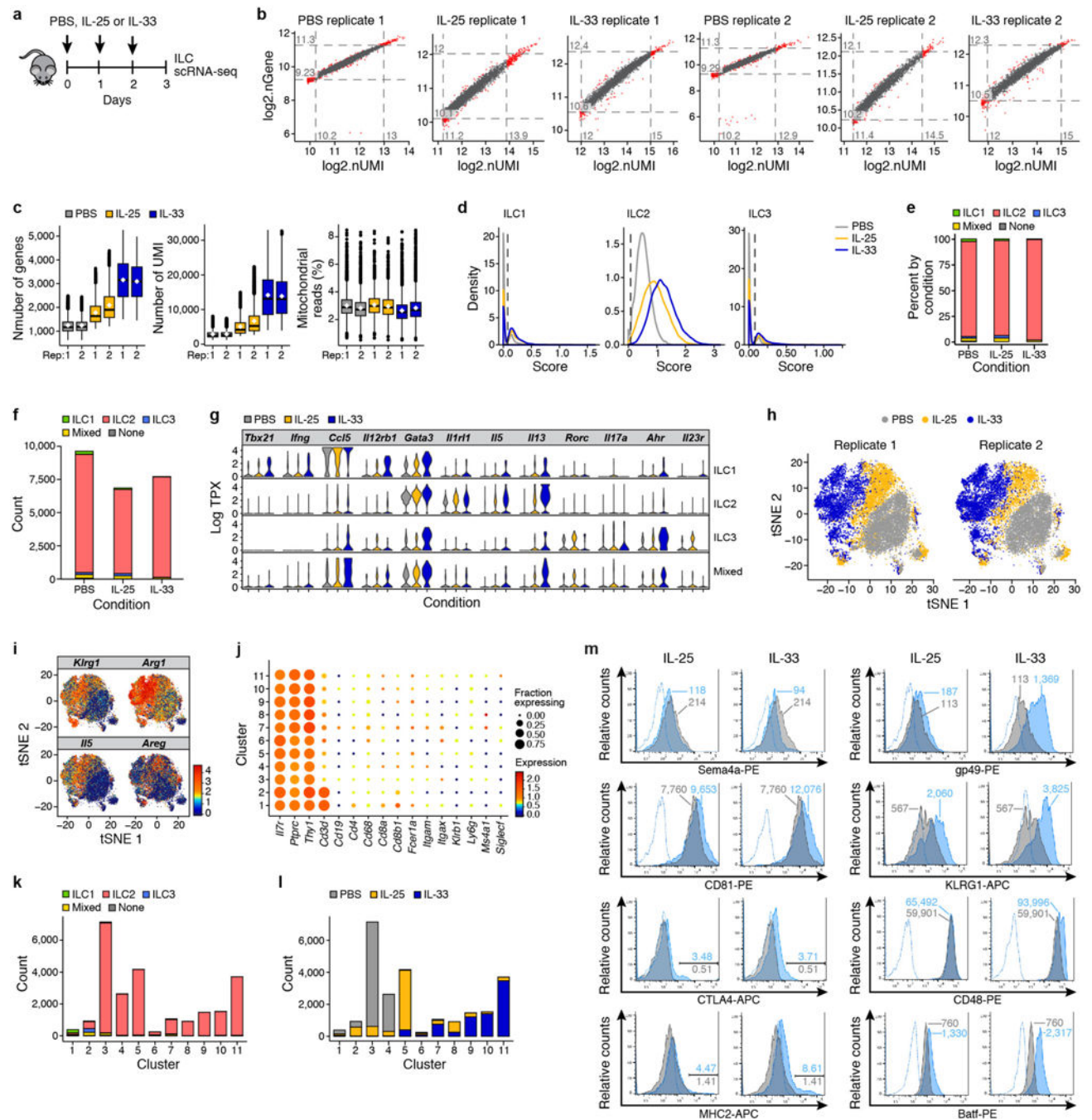
To rank the results for each model, we created a list of differentially expressed candidate genes that are detected in at least 30% of the cells in one of the groups in the model and have a coefficient for a term of interest with an absolute value at least 1.0 (for condition-based models) or 1.5 (for cluster models) and corresponding FDR-adjusted P values $<1 \times 10^{-4}$ (for condition-based models) or $<1 \times 10^{-5}$ (for cluster models). We ranked the candidates by lowest P value and by largest absolute value of coefficient. The top 40 genes (for condition model) or 3 genes (for cluster model) according to each ranking were reported, with a minimum of 10 genes (for condition model) or 1 gene (for cluster model), if available, selected from each of the set of candidates with positive coefficients and the set with negative coefficients (Supplementary Table 1). To create the plot in Fig. 2c, we took a high-ranked illustrative subset of these genes.

To compare plates and droplets, we took as the null set all genes (11,117 genes) detected in both group A from droplet-based data and in plates. For the PCA comparison, we took the union of the highest and lowest 10 (group A) or 20 (plates) genes for the PCs used in each analysis (141 genes from droplet-based data, 202 genes from plate-based data, 66 genes in the intersection), and used Fisher's exact test to determine significance ($P < 3.74 \times 10^{-80}$). For the comparison of differentially expressed genes, we used the previously computed sets of top-ranked DE genes for group A (219 genes) and for the plate data (72 genes), and again used Fisher's exact test to determine significance of the overlap ($P < 3.91 \times 10^{-25}$).

Re-annotation of the 3' UTR of *Nmur1*

Initially, *Nmur1* had essentially no detected expression in the droplet-based scRNA-seq data, though many reads align to a region just downstream of the *Nmur1* 3' UTR annotation (Extended Data Fig. 4b). To explore the basis of this discrepancy, we aligned long (75 bp) paired-end reads from full-length RNA-seq of population samples that included cells from all three stimulation conditions (only those from IL-25 shown). Many read alignments bridge the annotated *Nmur1* transcript and the region downstream where droplet-based 3' reads align (Extended Data Fig. 4b), evidence that *Nmur1* has isoforms longer than the annotated transcript. We re-annotated the transcriptome, moving the 3' end from 86,386,242 to 86,384,000, and realigned the droplet-based scRNA-seq data, resulting in a robust increase in frequency of detection of *Nmur1*. All droplet-based scRNA-seq data shown in this manuscript was aligned to this re-annotated transcriptome.

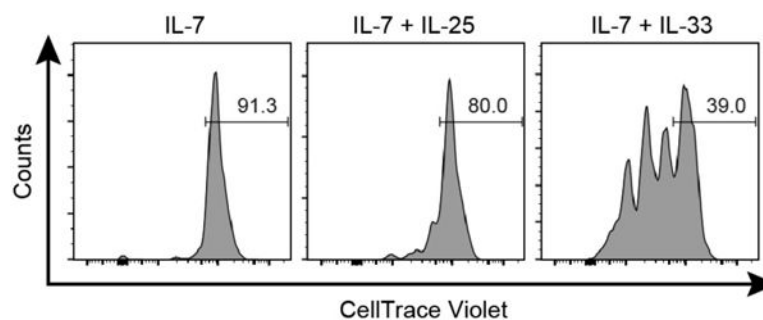
Extended Data



Extended Data Figure 1. Massively parallel scRNA-seq of lung ILCs

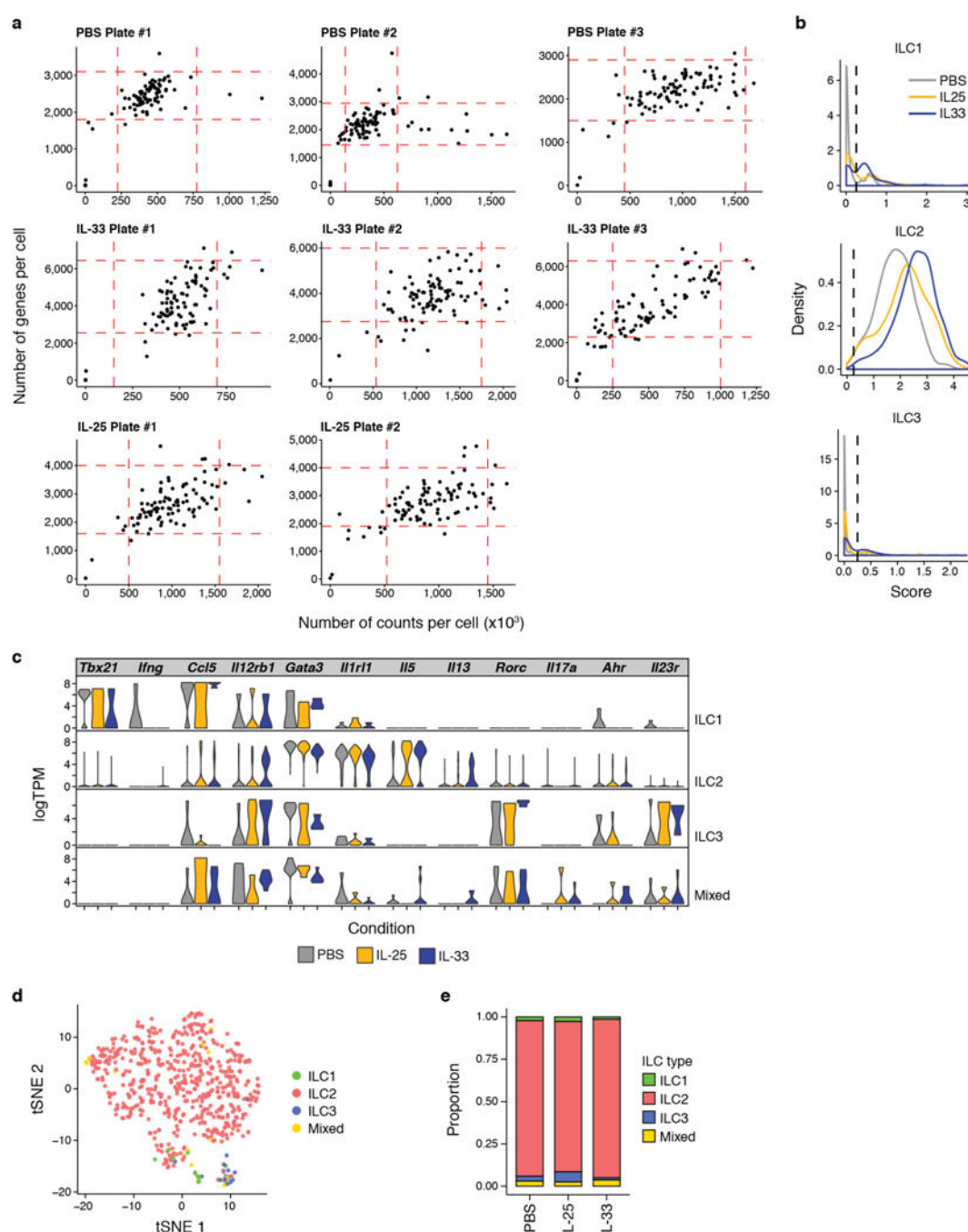
a, Schematic of experimental method for *in vivo* activation of ILCs. **b**, **c**, Quality measures. **b**, Scatter plots show for each cell the relation between the number of UMIs (nUMI, x axis) and the number of genes (nGene, y axis). Cells are coloured according to whether they are included (grey) or excluded (red) from further analysis by these measures. **c**, Box plots show the distribution of the number of unique genes (y axis, left), UMIs (y axis, middle) and per

cent of normalized expression from mitochondrial genes (*y* axis, right) in each treatment and replicate (rep; *x* axis). White diamond indicates the mean. **d–g**, ILC classification by signatures. **d**, Density plots show the distributions of ILC subset signature scores (*x* axis) for ILC1 (left), ILC2 (middle) and ILC3 (right) in each of three treatments (control, grey; IL-25, yellow; IL-33, blue). Dashed lines mark the cut-offs used in the ILC classification for each signature. **e**, Bar plots of the proportion of 24,187 cells (*y* axis) classified in each treatment (*x* axis) based on transcriptional signatures of known ILC subsets as ILC1 (green), ILC2 (pink), ILC3 (blue), mixed (yellow, scoring for two or more signatures), or none (grey, scoring for none of the three signatures). **f**, Bar plots show the number of ILCs (*y* axis) classified to each subset (colour code) in the PBS, IL-25 or IL-33 conditions (*x* axis). **g**, Expression of key ILC marker genes. Violin plots show the distribution of expression levels (logTPX, *y* axis) of each of 12 ILC marker genes (marked on top) in cells classified in each subtype (rows) in each treatment (*x* axis). **h**, Cell groupings are independent of batch. **h**, **i** SNE plot of cells (as in Fig. 1a) from replicate 1 (left plot) and replicate 2 (right plot), coloured by condition. **i**, Expression of key genes. **i** SNE is coloured by the relative expression of the indicated genes. **j**, Gene expression for marker genes of ILCs and other immune cell types. For each gene (columns) in each cluster (rows), the proportion of cells in the cluster expressing the gene (dot size) and the relative mean log nUMI of expressing cells (colour) is plotted. **k**, **l**, Cluster composition. Bar plots show the number of cells (*y* axis) from each ILC type (**k**) and condition (**l**) in each cluster (*x* axis). **m**, Validation of expression patterns identified by scRNA-seq using flow cytometry. In each histogram, the expression of proteins encoded by genes identified with scRNA-seq on ILCs from mice treated with PBS (grey, closed) versus one of the alarmins IL-25 or IL-33 (blue, closed) is shown, as well as a fluorescence minus one (FMO) control (blue, dashed). Numbers indicate the mean fluorescence intensity of the marker in PBS (grey) or condition (blue) or, for CTLA4 and MHC class II, the frequency of cells positive for the marker in PBS (grey) or condition (blue). Data are representative of at least two individual experiments.



Extended Data Figure 2. Alarmin-induced ILC proliferation *in vitro*

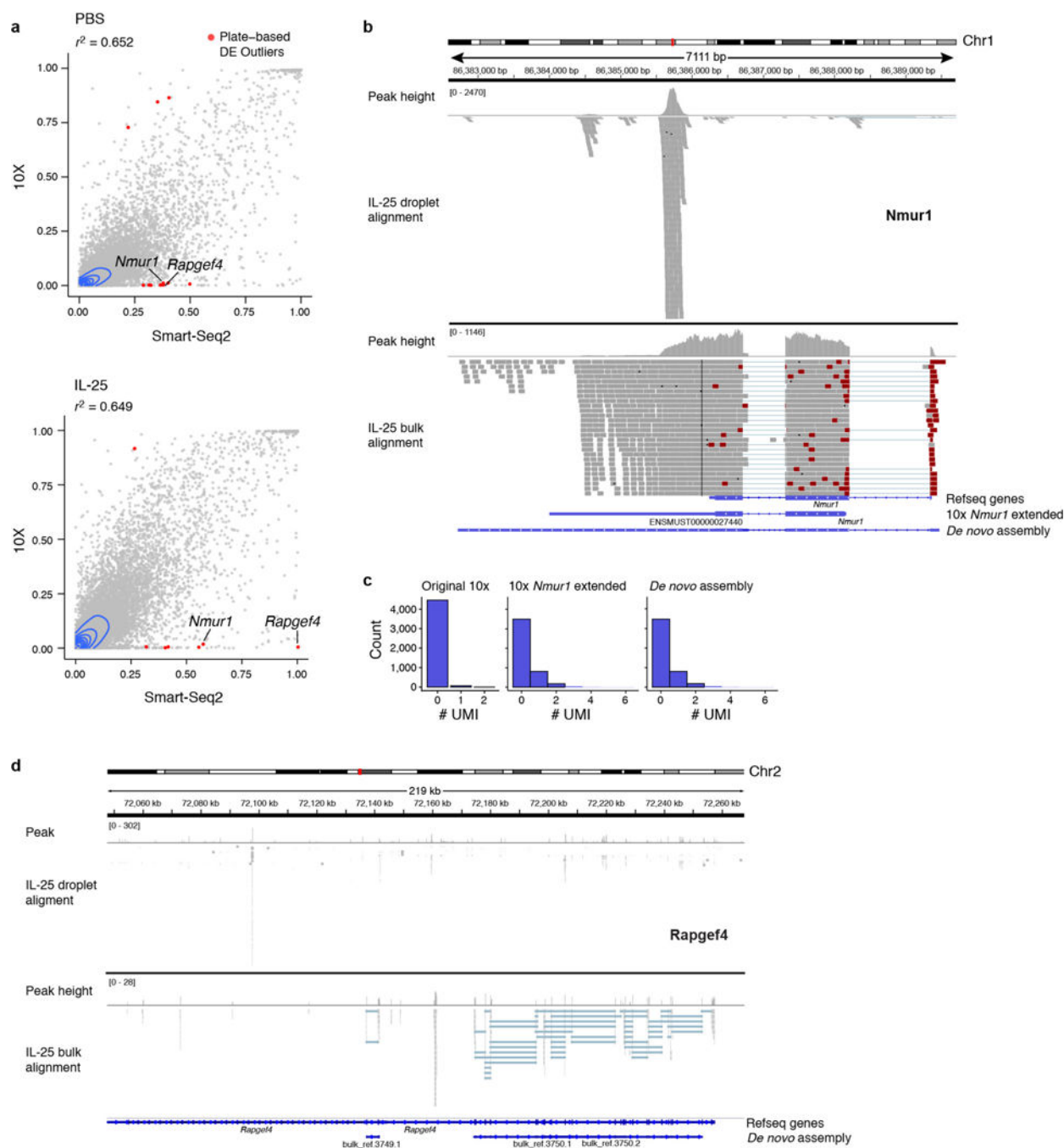
ILCs were labelled with CellTrace Violet and cultured *in vitro* under the indicated conditions. After 3 days, proliferation was analysed by flow cytometric analysis of CellTrace Violet dilution. The frequency of non-proliferating ILCs is indicated. Data are representative of two individual experiments.



Extended Data Figure 3. Plate-based scRNA-seq of lung-resident ILCs

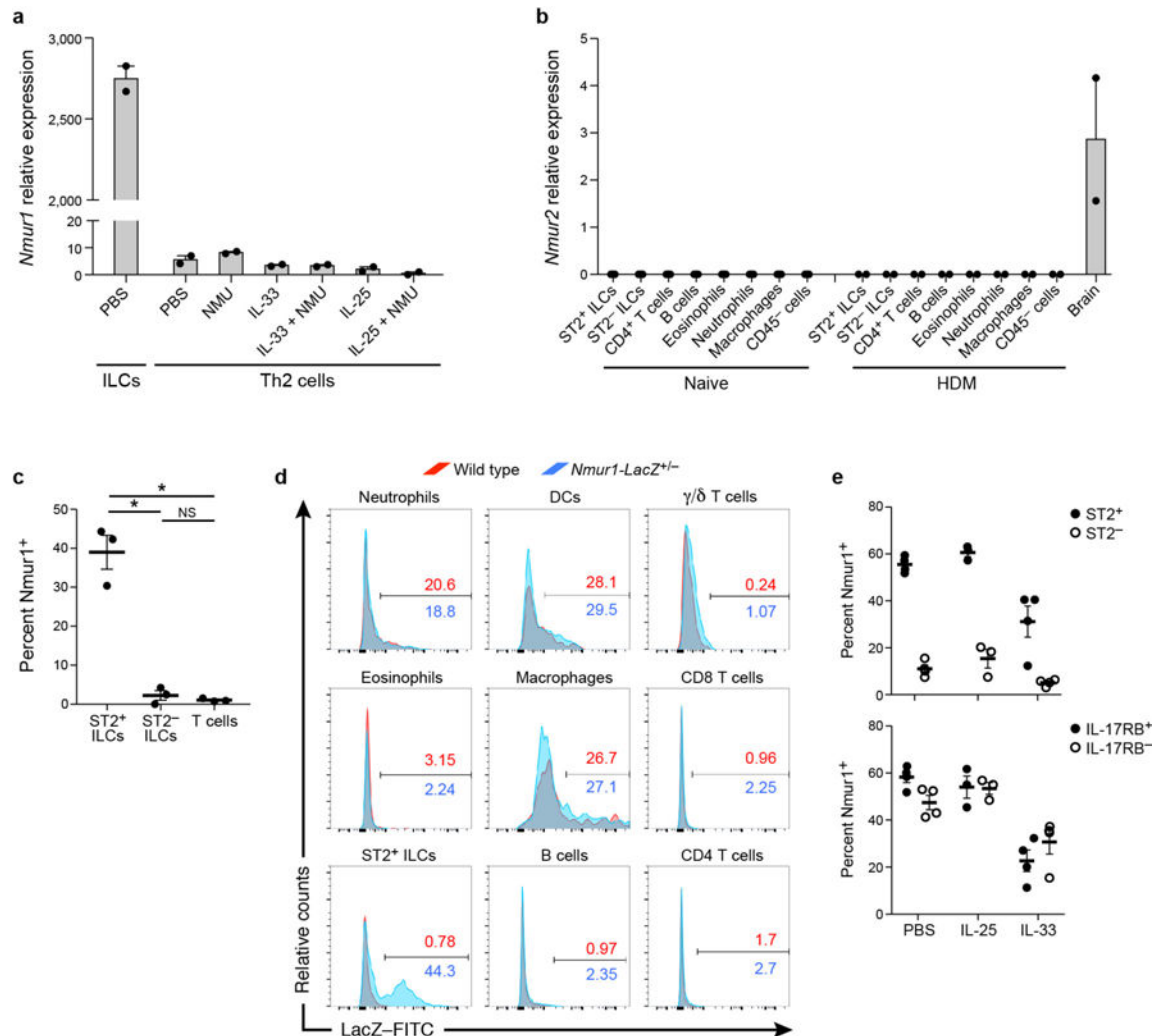
a, Quality measures. Scatter plots for each plate showing the total number of read counts per cell (x axis) and number of unique detected genes (y axis) in each cell. Dashed lines indicate cut-offs for passing quality control. Only cells in the central quadrant were retained for analysis. **b–e**, ILC subset classification. **b**, ILC signature score distributions. Density plots show the distributions of ILC subset signature scores (x axis) for ILC1 (top), ILC2 (middle) and ILC3 (bottom) in each of three treatments (control, grey; IL-25, yellow; IL-33, blue). Dashed lines mark the minimum score cut-off used in the ILC classification for each

signature. **c**, Expression of key ILC marker genes. Violin plots show the distribution of expression levels (logTPM, *y* axis) of each of 12 ILC marker genes (marked on top) in cells classified in each subtype (rows) in each treatment (*x* axis). **d**, Distinct cell subsets by ILC expression profile. tSNE plot shows individual cells (dots) in a nonlinear reduced representation of the top 9 PCs, with cells coloured by ILC subset. **e**, Composition by treatment condition. Bar plots show the proportion of each ILC subtype (*y* axis) in each treatment condition (*x* axis).



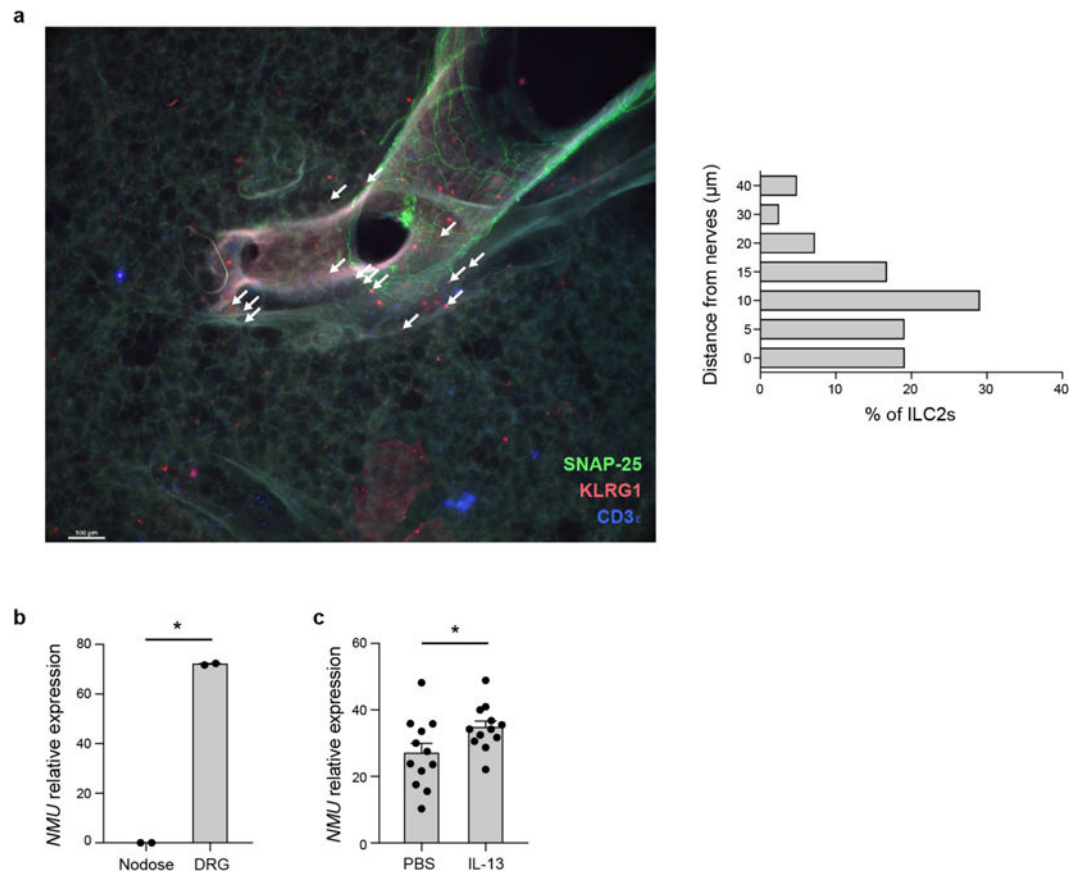
Extended Data Figure 4. Accurate detection of *Nmur1* from massively parallel 3' end scRNA-seq requires cell-type specific annotation

a, Comparison of gene expression estimates from plate-based and droplet-based scRNA-seq. Scatter plots show for each gene (dot) the fraction of cells expressing it according to plate-based scRNA-seq (x axis) and droplet-based scRNA-seq (y axis) in the PBS (top) and IL-25 (bottom) conditions. Of the differentially expressed genes in the plate-based data that are expressed in a substantially different proportion of cells compared to droplet-based data (red), *Nmur1* and *Rapgef4* are among the highest ranked and are only detected in the plate-based data. **b**, Re-annotation of the *Nmur1* locus by RNA-seq and assembly. Shown is a window of approximately 7 kb around the annotated *Nmur1* locus on chromosome 1 (top) along with read alignments to that region from either droplet-based 3' scRNA-seq (top, 55-nt reads) or from population (bulk) RNA-seq of ILCs (bottom, 75-nt reads). The Refseq annotation of *Nmur1* (top blue track) does not extend to the 3' end of the transcript, as defined by either the scRNA-seq reads (10× *Nmur1* extended; middle blue track) or by a transcriptome reassembly from bulk RNA-seq (StringTie reassembled; bottom blue track). **c**, Corrected annotation recovers *Nmur1*. Histogram shows the distribution of expression levels of *Nmur1* in single cells based on droplet-based scRNA-seq data when expression was calculated by aligning reads with the original RefSeq annotation (left), the scRNA-seq read-based extended annotation (middle) or the reassembled transcript annotation from bulk RNA-seq (right). **d**, *Rapgef4* locus correctly annotated. Shown is a plot for *Rapgef4*, arranged as in **b**. The 3' annotation in the RefSeq annotation agrees with the observed end from bulk RNA-seq.



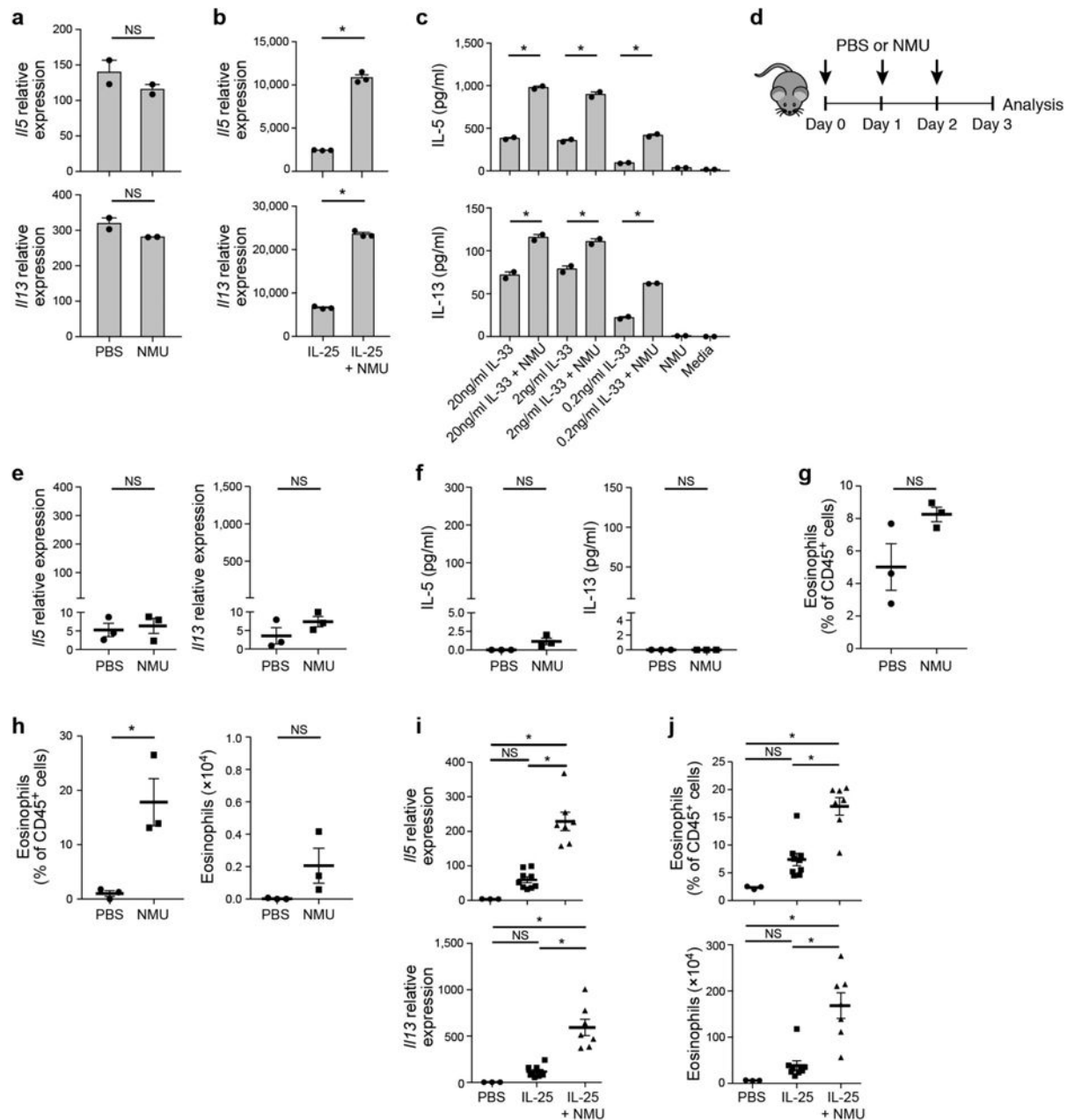
Extended Data Figure 5. Expression of *Nmur1* and *Nmur2* in lung-resident immune cells
a, Minimal expression of *Nmur1* on *in vitro* differentiated T_H2 cells. Bar chart shows *Nmur1* mRNA levels by qPCR in both T_H2 cells differentiated under the indicated conditions *in vitro*, and in freshly isolated ILCs. Data points represent technical replicates (*n* = 2). **b**, *Nmur2* is not expressed by lung-resident immune cells, including ILCs. Bar chart shows *Nmur2* mRNA levels by qPCR for the indicated cell types, which were sorted from mice either at steady state (PBS) or after HDM challenge. The mean of technical replicates is shown (*n* = 2). **c**, Summary graph of the flow cytometry data, of which a representative is shown in Fig. 2e. Plot shows the frequency of NMUR1⁺ cells in different cell populations from *Nmur1*-LacZ reporter mice as assayed by flow cytometry. Data points represent individual mice (*n* = 3). **d**, *Nmur1*-LacZ β-galactosidase activity reveals ILC-specific NMUR1 expression. Representative histograms show the distribution of expression of NMUR1 in the indicated cell types as determined by flow cytometry in cells isolated from wild-type (red) and *Nmur1*-LacZ heterozygous (blue) mice. The frequency of *Nmur1*-LacZ-positive cells is indicated. **e**, NMUR1 is preferentially expressed by ST2⁺ ILCs. The expression of ST2, IL-17RB and NMUR1 was analysed by flow cytometry, and the

frequency of NMUR1⁺ ILCs within the indicated populations is shown. Each data point reflects an individual mouse ($n = 4$ for PBS and IL-33; $n = 3$ for IL-25). All panels represent one of two individual experiments, mean is indicated, error bars represent s.e.m.; * $P < 0.05$ by two-tailed t -test.



Extended Data Figure 6. ILCs and neurons are in proximity in the lung, and NMU is expressed by dorsal root ganglion neurons

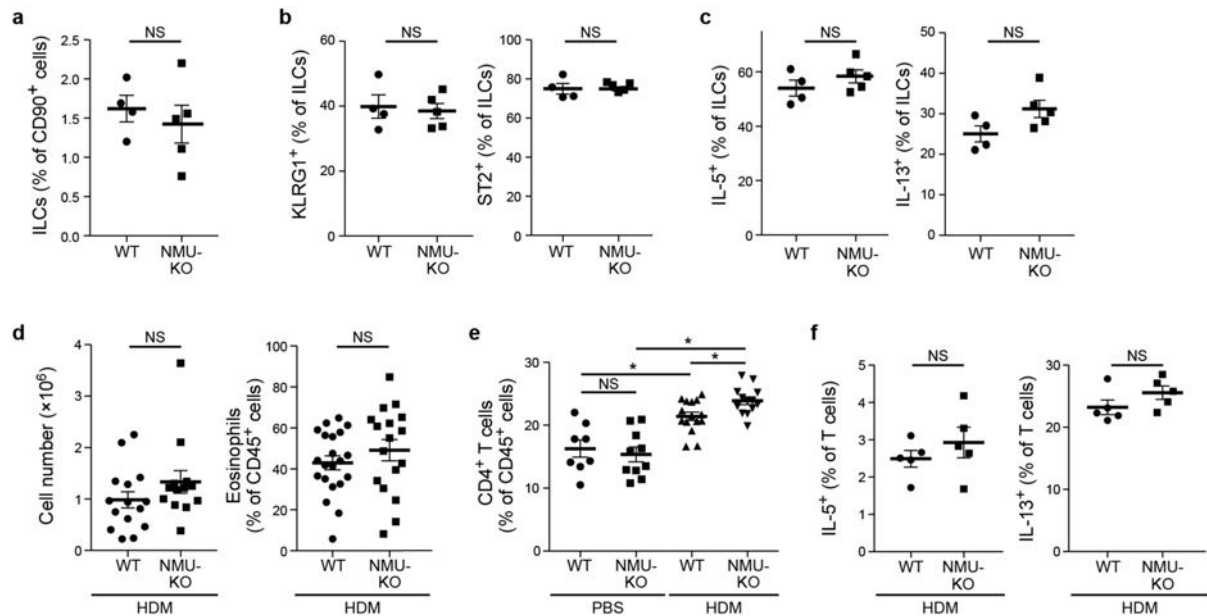
a, Representative image (left) of lung sections stained for the neuronal marker SNAP-25 (green), KLRG1 (red), and CD3ε (blue). Arrows indicate KLRG1⁺ CD3ε⁻ cells in close proximity to SNAP-25⁺ nerve fibres. Scale bar, 100 μm. Bar plot (right) shows the frequency of ILCs (x axis) within indicated distances (y axis) of SNAP-25⁺ nerve fibres. All KLRG1⁺CD3ε⁻ cells in the field of view were counted, and the distances between ILCs and the closest SNAP-25⁺ nerve fibre were measured (3–5 lung sections per mouse, $n = 3$ mice). Data are representative of three independent experiments with similar results. **b**, **c**, NMU is expressed in thoracic dorsal root ganglion (DRG) neurons. NMU expression was examined by qPCR. **b**, NMU expression in the nodose/jugular ganglion and DRG *ex vivo*. Data points represent technical replicates ($n = 2$). **c**, NMU expression in DRG neurons stimulated *in vitro* with IL-13. Data points represent two technical replicates from each of six biologic replicates. All panels are representative of at least two individual experiments, mean is indicated, error bars represent s.e.m.; * $P < 0.05$ by two-tailed t -test.



Extended Data Figure 7. NMU induces minimal lung inflammation in the absence of alarmins

a, NMU does not alter *in vitro* expression of type 2 cytokines in T cells. Expression of *IL5* and *IL13* is similar in T_H2 cells cultured with or without NMU, as assessed by qPCR. **b**, **c**, ILCs were isolated from naive mice and cultured *in vitro* with the indicated stimuli. **b**, ILCs cultured *in vitro* have markedly enhanced *IL5* and *IL13* mRNA expression in response to combination of NMU and IL-25, as measured by qPCR. **c**, IL-33-induced IL-5 and IL-13 secretion is enhanced by NMU, as determined by LegendPlex. Data points represent technical replicates, and the mean is indicated. **d–h**, NMU alone induces minimal allergic lung inflammation. **d**, Schematic of experimental method for activation of ILCs with NMU *in vivo*. **e**, *IL5* and *IL13* expression was determined in lung mononuclear cells by qPCR. **f**,

The concentration of IL-5 and IL-13 protein in BALF was analysed by LegendPlex. **g, h**, Eosinophil frequencies in lung parenchyma (**g**) and BALF (**h**, left), and BALF eosinophil numbers (**h**, right), as determined by flow cytometry. Data points correspond to individual mice ($n = 3$). **i**, The combination of IL-25 combined with NMU markedly enhanced *Il5* (top) and *Il13* (bottom) mRNA expression in lung mononuclear cells, as measured by qPCR. **j**, NMU and IL-25 synergize to promote tissue eosinophilia. Eosinophil frequency (top) and number (bottom) in lung parenchyma was assessed by flow cytometry. Data points correspond to individual mice (PBS, $n = 3$; IL-25, $n = 9$; IL-25 combined with NMU, $n = 7$). For all panels, data are representative of at least two individual experiments, mean is indicated, error bars represent s.e.m.; * $P < 0.05$ by two-tailed t -test.



Extended Data Figure 8. Phenotype of *Nmu*-knockout mice

a–c, ILC frequency and function are not altered in the absence of NMU in steady state.

Lung-resident ILCs isolated from wild-type and NMU-deficient mice were analysed by flow cytometry. **a, b**, The frequency of ILCs (among CD90⁺ cells, **a**) and expression of KLRG1 and ST2 on ILCs (**b**) are unchanged in *Nmu*-knockout mice compared to control mice. **c**,

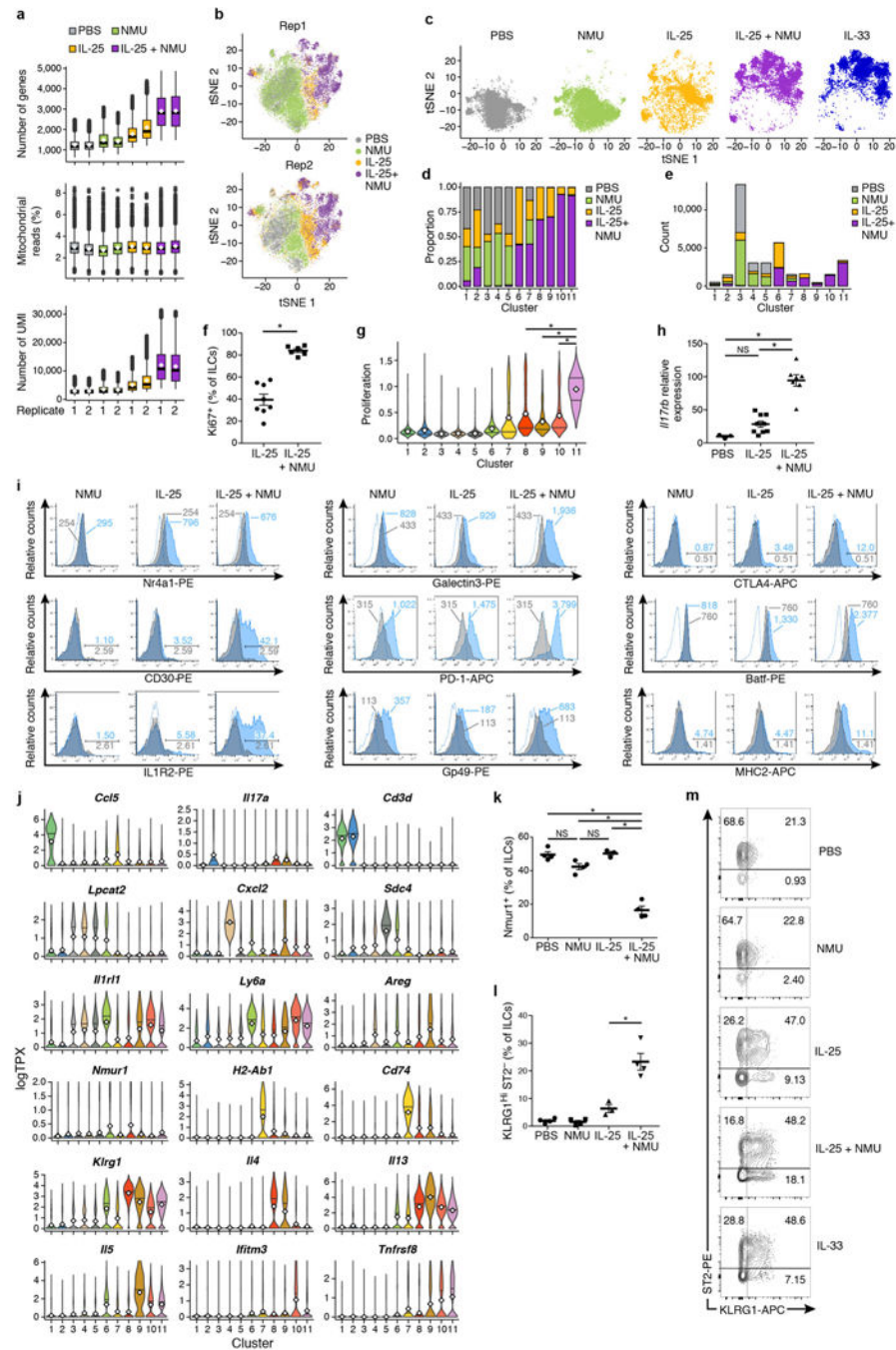
Frequency of IL-5- and IL-13-producing ILCs in *Nmu*-knockout mice is comparable to that of control mice. Each data point corresponds to an individual mouse (wild-type, $n = 4$; *Nmu*-knockout, $n = 5$).

d–f, Analysis of BALF and T-cell responses in *Nmu*-knockout mice after HDM challenge. **d**, BALF cell numbers (left) and the frequency of eosinophils (right) were analysed after HDM challenge in *Nmu*-knockout mice. Total cell numbers (wild-type, $n = 15$; *Nmu*-knockout, $n = 13$) and eosinophil frequency are unchanged in *Nmu*-knockout mice

($n = 17$) compared to wild-type mice ($n = 21$). **e**, Increased lung-infiltrating CD4 T cells in the absence of NMU. The frequency of lung-infiltrating T cells was determined by flow cytometry after HDM challenge (wild-type, $n = 15$; *Nmu*-knockout, $n = 13$). **f**, Intact T_H2 response in the absence of NMU. Expression of IL-5 and IL-13 by CD4 T cells was

analysed by flow cytometry following HDM challenge. Each data point represents an individual mouse (wild-type, $n = 5$; *Nmu*-knockout, $n = 5$). All panels are representative of

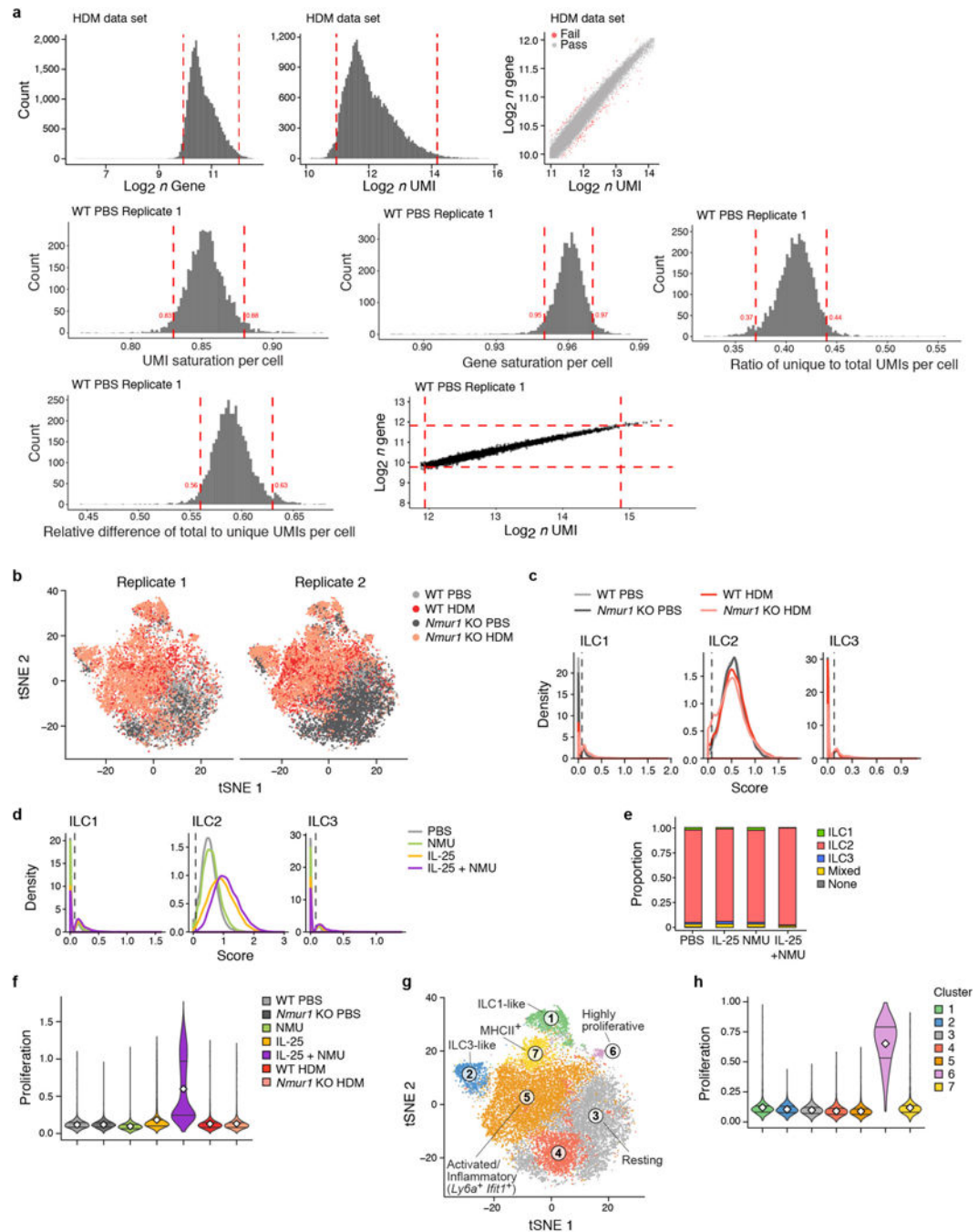
at least two individual experiments. For all panels, mean is indicated, error bars represent s.e.m.; * $P < 0.05$ by two-tailed t -test (a–d, f) or one-way ANOVA (e).



Extended Data Figure 9. Massively parallel, droplet-based scRNA-seq of ILCs from mice treated with NMU or IL-25 combined with NMU

a, Quality measures. Bar plots show the distribution of the number of unique genes (y axis, top), per cent of reads from mitochondrial genes (y axis, middle) and number of UMIs (y axis, bottom) in each treatment and replicate (x axis). White diamond indicates the mean. **b**, Grouping of ILCs is independent of batch. tSNE plots (as in Fig. 4a) of cells from replicate 1

(top) and replicate 2 (bottom) coloured by condition. **c**, Faceted *t*SNE plot of ILCs from all alarmin and NMU treatments, coloured by condition, shows that IL-25 combined with NMU and IL-33 induce partially overlapping transcriptional responses. **d, e**, Cluster composition. **d**, Bar plot shows the proportion of ILCs from each condition in each cluster. **e**, Bar plot shows the number of cells from each condition in each cluster. **f, g**, IL-25 combined with NMU promotes ILC proliferation. **f**, The frequency of Ki-67⁺ ILCs was determined by flow cytometry in mice treated with IL-25 or IL-25 combined with NMU. Data points represent individual mice (IL-25, *n* = 8; IL-25 combined with NMU, *n* = 6). **g**, Violin plots show the distributions of the proliferation signature scores (*y* axis) for the cells in each cluster (*x* axis) (white diamond, mean; lines, first and third quartiles). Proliferation scores in cluster 11 are significantly higher than those in the other clusters dominated by IL-25 combined with NMU (8, 9 and 10) (*t*-test, $P < 2.2 \times 10^{-16}$). **h**, IL-25 combined with NMU enhances expression of *Il17rb* in mononuclear lung cells, as shown by qPCR. Data points represent individual mice (PBS, *n* = 3; IL-25, *n* = 9; IL-25 combined with NMU, *n* = 7). **i**, Validation of expression patterns identified by scRNA-seq using flow cytometry. Expression levels for proteins encoded by genes identified by scRNA-seq on ILCs from mice treated with PBS (grey, closed histogram) versus one of the treatments (blue, closed histogram), as well as an FMO control (dashed open histogram) is shown. Numbers indicate the mean fluorescence intensity of the respective marker or, if a gate is indicated, the frequency of positive ILCs in PBS (grey) and in the indicated condition (blue). **j**, Distinct patterns of expression of key differentially expressed genes across clusters. Violin plots show the expression levels in logTPX (*y* axis) for the indicated genes across the cells in each cluster (*x* axis) (white diamond, mean; line, median). **k**, NMUR1 is downregulated after activation with IL-25 combined with NMU. The frequency of NMUR1⁺ ILCs (*y* axis) in each condition among ILCs isolated from mice treated with the indicated stimuli is shown. Dots represent individual mice (*n* = 4, except for IL-25, where *n* = 3). **l, m**, Increased frequency of KLRG1^{hi}ST2⁻ inflammatory ILC2s (iILC2s) after treatment with IL-25 combined with NMU. **l**, Frequency of iILC2s (of total ILCs) isolated from mice after different treatments. Dots represent individual mice (*n* = 4, except for IL-25, where *n* = 3). **m**, Representative flow cytometry plots of ST2 and KLRG1 expression on ILCs for the indicated conditions. For panels **f, h, k, l**, mean is indicated and error bars represent s.e.m.; **P* < 0.05 by two-tailed *t*-test (**f**) or one-way ANOVA (**h, k, l**).



Extended Data Figure 10. Transcriptional analysis by massively parallel scRNA-seq of ILCs from wild-type and *Nmur1*-knockout mice during airway inflammation

a, Quality measures. The top row shows the distributions of the number of genes (log scale, x axis, left histogram) and UMIs (log scale, x axis, centre histogram) per cell and their relation (scatter plot, right) in the aggregated data. The middle row shows the distributions of the estimated saturation for UMIs (x axis, left histogram) and genes (x axis, middle histogram) per cell, as well as the ratio of the number of unique UMIs to total number of UMIs per cell (x axis, right histogram), for a representative sample. The bottom row shows

the distribution of the relative difference of the total number of UMIs and number of unique UMIs (x axis, left histogram), and the relation between the number of UMIs and number of genes (scatter plot, right), for the same representative sample. Dashed lines show lower and upper cut-offs used. Outlier cells (red dots, scatter plot) were also removed. **b**, Minor batch effects. t SNE plots show cells from replicate 1 (left) and replicate 2 (right) coloured by condition and genotype (PBS-treated wild-type mice (light grey), HDM-treated wild-type mice (red), PBS-treated *Nmur1*-knockout mice (dark grey), HDM-treated *Nmur1*-knockout mice (salmon)). **c, d**, Signature-based scoring of ILCs. Density plots show the distribution of scores for ILC1, 2 and 3 signatures in the cells from indicated treatment conditions. Dashed line indicates the cut-off for each signature used in assigning ILC type. **e**, Composition by ILC type. Bar plot shows proportion of each ILC type in the conditions indicated. **f**, ILC proliferation is strongly increased by IL-25 combined with NMU. Violin plots show the distribution of proliferation scores (y axis) across the cells in indicated conditions (x axis) (white diamond, mean; lines, first and third quartiles). **g**, Similar clusters are induced by HDM and by IL-25 combined with NMU treatment. t SNE plot shows ILCs from PBS- and HDM-treated wild-type and *Nmur1*-knockout mice (as in Fig. 5a), coloured by cluster and labelled by post hoc annotations. Note similarity to clustering in Fig. 4b. **h**, Cluster-specific ILC proliferation in cells from HDM-treated mice. Violin plots show the distribution of proliferation scores (y axis) across the cells in each cluster (x axis), as in **g**.

Supplementary Material

Refer to Web version on PubMed Central for supplementary material.

Acknowledgments

We thank J. Xia, G. Zhu, D. Kozoriz, the Dana Farber Cancer Institute Rodent Histopathology Core, and the Harvard Medical School Transgenic Core for technical expertise. The KOMP repository, CSD Consortium, and Velocigene at Regeneron Inc. generated *Nmur1*-LacZ mice with the support of the NIH (U01HG004085, U01HG004080). M. Kojima (Kurume University) generated *Nmu* knockout mice. L. Gaffney assisted with figure preparation. R. Herbst and A. Haber provided statistical advice. A.W. is jointly supervised by V.K.K. and H.-M. Jäck (Friedrich-Alexander University of Erlangen-Nürnberg, Erlangen, Germany) and is supported by a Boehringer Ingelheim Fonds PhD fellowship. P.R.B. (1K08AI123516), R.E.A. (1K08HL130540), B.D.L. (RO1-HL122531) and V.K.K. (PO1 AI056299, AI039671) are supported by the N.I.H. M.S.K. was supported by Charles A. King Trust Postdoctoral Research Fellowship Program and the Simeon J. Fortin Charitable Foundation. C.S.N.K. is supported by the German Research Foundation (DFG; KL 2963/1-1). T.M. is supported by the Crohn's and Colitis Foundation of America (CCFA). D.A. is supported by the NIH (AI061570, AI087990, AI074878, AI083480, AI095466, AI095608, AI102942 and AI097333), the Burroughs Wellcome Fund, and the CCFA. A.R. is an Investigator of the Howard Hughes Medical Institute. We acknowledge the support of the Food Allergy Scientific Initiative and the Klarman Cell Observatory at the Broad Institute.

References

1. Cheng D, et al. Epithelial interleukin-25 is a key mediator in Th2-high, corticosteroid-responsive asthma. *Am J Respir Crit Care Med*. 2014; 190:639–648. [PubMed: 25133876]
2. Huang Y, et al. IL-25-responsive, lineage-negative KLRG1^{hi} cells are multipotential 'inflammatory' type 2 innate lymphoid cells. *Nat Immunol*. 2015; 16:161–169. [PubMed: 25531830]
3. Gudbjartsson DF, et al. Sequence variants affecting eosinophil numbers associate with asthma and myocardial infarction. *Nat Genet*. 2009; 41:342–347. [PubMed: 19198610]
4. Halim TY, et al. Group 2 innate lymphoid cells are critical for the initiation of adaptive T helper 2 cell-mediated allergic lung inflammation. *Immunity*. 2014; 40:425–435. [PubMed: 24613091]

5. Salimi M, et al. A role for IL-25 and IL-33-driven type-2 innate lymphoid cells in atopic dermatitis. *J Exp Med*. 2013; 210:2939–2950. [PubMed: 24323357]
6. Moro K, et al. Innate production of T(H)2 cytokines by adipose tissue-associated c-Kit⁺Sca⁻¹ lymphoid cells. *Nature*. 2010; 463:540–544. [PubMed: 20023630]
7. Neill DR, et al. Nuocytes represent a new innate effector leukocyte that mediates type-2 immunity. *Nature*. 2010; 464:1367–1370. [PubMed: 20200518]
8. Chang YJ, et al. Innate lymphoid cells mediate influenza-induced airway hyper-reactivity independently of adaptive immunity. *Nat Immunol*. 2011; 12:631–638. [PubMed: 21623379]
9. Monticelli LA, et al. Innate lymphoid cells promote lung-tissue homeostasis after infection with influenza virus. *Nat Immunol*. 2011; 12:1045–1054. [PubMed: 21946417]
10. Tanay A, Regev A. Scaling single-cell genomics from phenomenology to mechanism. *Nature*. 2017; 541:331–338. [PubMed: 28102262]
11. Wagner A, Regev A, Yosef N. Revealing the vectors of cellular identity with single-cell genomics. *Nat Biotechnol*. 2016; 34:1145–1160. [PubMed: 27824854]
12. Gaublot JM, et al. Single-cell genomics unveils critical regulators of Th17 cell pathogenicity. *Cell*. 2015; 163:1400–1412. [PubMed: 26607794]
13. Habib N, et al. Div-Seq: single-nucleus RNA-seq reveals dynamics of rare adult newborn neurons. *Science*. 2016; 353:925–928. [PubMed: 27471252]
14. Shekhar K, et al. Comprehensive classification of retinal bipolar neurons by single-cell transcriptomics. *Cell*. 2016; 166:1308–1323.e30. [PubMed: 27565351]
15. Gury-BenAri M, et al. The spectrum and regulatory landscape of intestinal innate lymphoid cells are shaped by the microbiome. *Cell*. 2016; 166:1231–1246.e13. [PubMed: 27545347]
16. Monticelli LA, et al. Arginase 1 is an innate lymphoid-cell-intrinsic metabolic checkpoint controlling type 2 inflammation. *Nat Immunol*. 2016; 17:656–665. [PubMed: 27043409]
17. Robinette ML, et al. Transcriptional programs define molecular characteristics of innate lymphoid cell classes and subsets. *Nat Immunol*. 2015; 16:306–317. [PubMed: 25621825]
18. Björklund AK, et al. The heterogeneity of human CD127⁺ innate lymphoid cells revealed by single-cell RNA sequencing. *Nat Immunol*. 2016; 17:451–460. [PubMed: 26878113]
19. Kowalczyk MS, et al. Single-cell RNA-seq reveals changes in cell cycle and differentiation programs upon aging of hematopoietic stem cells. *Genome Res*. 2015; 25:1860–1872. [PubMed: 26430063]
20. Tirosh I, et al. Dissecting the multicellular ecosystem of metastatic melanoma by single-cell RNA-seq. *Science*. 2016; 352:189–196. [PubMed: 27124452]
21. Dixit A, et al. Perturb-Seq: dissecting molecular circuits with scalable single-cell RNA profiling of pooled genetic screens. *Cell*. 2016; 167:1853–1866.e17. [PubMed: 27984732]
22. Zheng GX, et al. Massively parallel digital transcriptional profiling of single cells. *Nat Commun*. 2017; 8:14049. [PubMed: 28091601]
23. Picelli S, et al. Smart-seq2 for sensitive full-length transcriptome profiling in single cells. *Nat Methods*. 2013; 10:1096–1098. [PubMed: 24056875]
24. Moriyama M, et al. The neuropeptide neuromedin U activates eosinophils and is involved in allergen-induced eosinophilia. *Am J Physiol Lung Cell Mol Physiol*. 2006; 290:L971–L977. [PubMed: 16373672]
25. Hedrick JA, et al. Identification of a human gastrointestinal tract and immune system receptor for the peptide neuromedin U. *Mol Pharmacol*. 2000; 58:870–875. [PubMed: 10999960]
26. Szekeres PG, et al. Neuromedin U is a potent agonist at the orphan G protein-coupled receptor FM3. *J Biol Chem*. 2000; 275:20247–20250. [PubMed: 10811630]
27. Shan L, et al. Identification of a novel neuromedin U receptor subtype expressed in the central nervous system. *J Biol Chem*. 2000; 275:39482–39486. [PubMed: 11010960]
28. Talbot S, et al. Silencing nociceptor neurons reduces allergic airway inflammation. *Neuron*. 2015; 87:341–354. [PubMed: 26119026]
29. Nussbaum JC, et al. Type 2 innate lymphoid cells control eosinophil homeostasis. *Nature*. 2013; 502:245–248. [PubMed: 24037376]

30. Audrit KJ, Delventhal L, Aydin Ö, Nassenstein C. The nervous system of airways and its remodeling in inflammatory lung diseases. *Cell Tissue Res.* 2017; 367:571–590. [PubMed: 28091773]
31. Polte T, Behrendt AK, Hansen G. Direct evidence for a critical role of CD30 in the development of allergic asthma. *J Allergy Clin Immunol.* 2006; 118:942–948. [PubMed: 17030250]
32. Schuliga M, et al. Plasminogen-stimulated inflammatory cytokine production by airway smooth muscle cells is regulated by annexin A2. *Am J Respir Cell Mol Biol.* 2013; 49:751–758. [PubMed: 23721211]
33. Heshmat NM, El-Hadidi ES. Soluble CD30 serum levels in atopic dermatitis and bronchial asthma and its relationship with disease severity in pediatric age. *Pediatr Allergy Immunol.* 2006; 17:297–303. [PubMed: 16771784]
34. Katsunuma T, et al. Analysis of gene expressions of T cells from children with acute exacerbations of asthma. *Int Arch Allergy Immunol.* 2004; 134:29–33. [PubMed: 15051937]
35. Sekigawa T, et al. Gene-expression profiles in human nasal polyp tissues and identification of genetic susceptibility in aspirin-intolerant asthma. *Clin Exp Allergy.* 2009; 39:972–981. [PubMed: 19489917]
36. Kurakula K, et al. Nuclear receptor Nur77 attenuates airway inflammation in mice by suppressing NF- κ B activity in lung epithelial cells. *J Immunol.* 2015; 195:1388–1398. [PubMed: 26170382]
37. Modena BD, et al. Gene expression correlated with severe asthma characteristics reveals heterogeneous mechanisms of severe disease. *Am J Respir Crit Care Med.* 2017; 195:1449–1463. [PubMed: 27984699]
38. Beale J, et al. Rhinovirus-induced IL-25 in asthma exacerbation drives type 2 immunity and allergic pulmonary inflammation. *Sci Transl Med.* 2014; 6:256ra134.
39. von Moltke J, Ji M, Liang HE, Locksley RM. Tuft-cell-derived IL-25 regulates an intestinal ILC2-epithelial response circuit. *Nature.* 2016; 529:221–225. [PubMed: 26675736]
40. Gerbe F, et al. Intestinal epithelial tuft cells initiate type 2 mucosal immunity to helminth parasites. *Nature.* 2016; 529:226–230. [PubMed: 26762460]
41. Howitt MR, et al. Tuft cells, taste-chemosensory cells, orchestrate parasite type 2 immunity in the gut. *Science.* 2016; 351:1329–1333. [PubMed: 26847546]
42. Gu X, et al. Chemosensory functions for pulmonary neuroendocrine cells. *Am J Respir Cell Mol Biol.* 2014; 50:637–646. [PubMed: 24134460]
43. Branchfield K, et al. Pulmonary neuroendocrine cells function as airway sensors to control lung immune response. *Science.* 2016; 351:707–710. [PubMed: 26743624]
44. Prendergast CE, Morton MF, Figueroa KW, Wu X, Shankley NP. Species-dependent smooth muscle contraction to Neuromedin U and determination of the receptor subtypes mediating contraction using NMU1 receptor knockout mice. *Br J Pharmacol.* 2006; 147:886–896. [PubMed: 16474416]
45. Singer M, et al. A distinct gene module for dysfunction uncoupled from activation in tumor-infiltrating T cells. *Cell.* 2016; 166:1500–1511.e9. [PubMed: 27610572]
46. Jäger A, Dardalhon V, Sobel RA, Bettelli E, Kuchroo VK. Th1, Th17, and Th9 effector cells induce experimental autoimmune encephalomyelitis with different pathological phenotypes. *J Immunol.* 2009; 183:7169–7177. [PubMed: 19890056]
47. Satija R, Farrell JA, Gennert D, Schier AF, Regev A. Spatial reconstruction of single-cell gene expression data. *Nat Biotechnol.* 2015; 33:495–502. [PubMed: 25867923]
48. Zeileis A, Kleiber C, Jackman S. Regression models for count data in R. *J Stat Softw.* 2008; 27
49. Jackman, S. *pscl: Classes and Methods for R Developed in the Political Science Computational Laboratory*, Stanford University. Department of Political Science, Stanford University; Stanford, California: R package version 1.4.9. <http://pscl.stanford.edu/>
50. Bray NL, Pimentel H, Melsted P, Pachter L. Near-optimal probabilistic RNA-seq quantification. *Nat Biotechnol.* 2016; 34:525–527. [PubMed: 27043002]
51. Soneson C, Love MI, Robinson MD. Differential analyses for RNA-seq: transcript-level estimates improve gene-level inferences. *F1000 Res.* 2015; 4:1521.

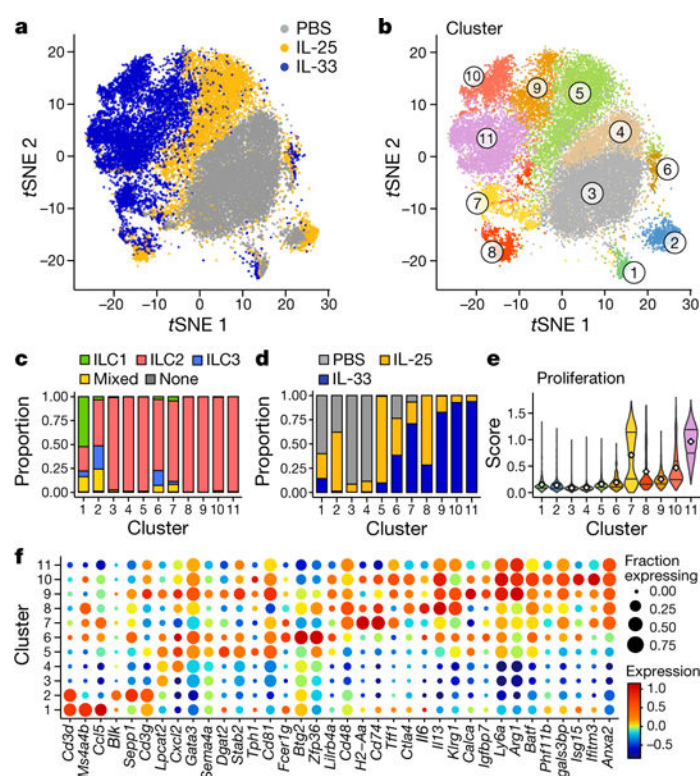


Figure 1. IL-25 and IL-33 induce multiple distinct transcriptional programs in ILCs

ILCs were profiled by droplet-based scRNA-seq. **a, b**, *t*-Distributed stochastic neighbour embedding (tSNE) plots show 24,187 cells (dots) in a nonlinear representation of the top 22 principal components (PCs). Cells are coloured by *in vivo* treatment (**a**) or cluster (**b**). **c, d**, Clustering reflects ILC type and treatment. Proportions of ILC subsets (**c**) or treatment condition (**d**) within each cluster. **e**, Distribution of proliferation scores by cluster. Diamond indicates the mean; lines, first and third quartiles. **f**, Representative differentially expressed genes (*x* axis) by cluster (*y* axis). Dot size represents the fraction of cells in the cluster that express the gene; colour indicates the mean expression (logTPX (see Methods)) in expressing cells, relative to other clusters.

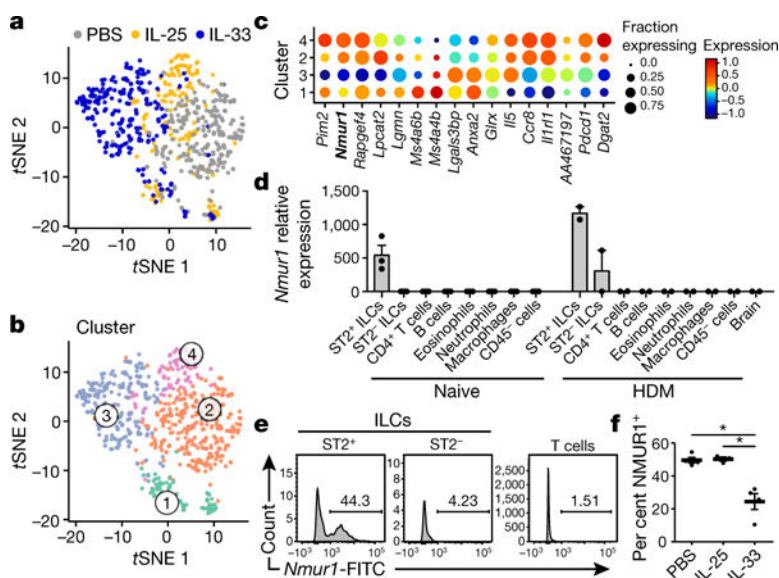


Figure 2. ScRNA-seq identifies *Nmur1* as a novel ILC2-specific gene

a–c, Full-length scRNA-seq. **a**, **b**, tSNE plots of 606 cells coloured by *in vivo* treatment (**a**) and cell clusters (**b**). **c**, Differentially expressed genes by cluster. *Nmur1* is indicated in bold. **d**, *Nmur1* expression by qPCR of lung-resident cell types isolated from control or HDM-challenged mice. Data points are technical replicates (PBS, $n = 3$; HDM, $n = 2$). **e**, Representative flow cytometry histograms of NMUR1 expression on the indicated cell types. **f**, Frequency of NMUR1⁺ ILCs determined by flow cytometry after the indicated treatments. Data points are individual mice (PBS and IL-33, $n = 4$; IL-25, $n = 3$). Data in panels **d**, **f** are representative of two individual experiments. Mean is indicated. Error bars, s.e.m.; * $P < 0.05$ (one-way ANOVA).

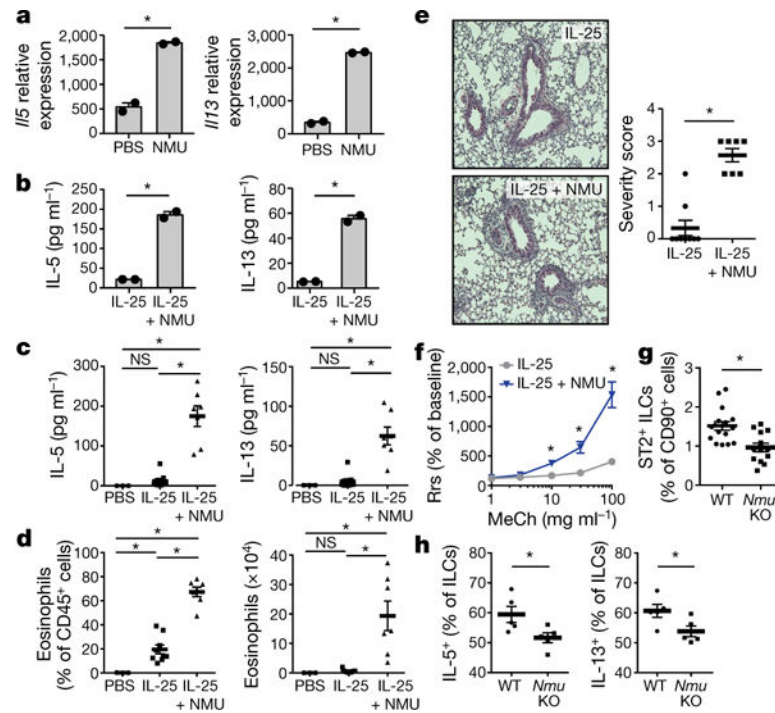


Figure 3. NMU amplifies IL-25-induced allergic inflammation

a, b, IL-5 and IL-13 levels in cultured ILCs. **a**, RNA levels determined by qPCR. **b**, Protein concentration determined by LegendPlex (see Methods). One of three independent experiments is shown. Data points are technical replicates ($n = 2$). **c**, BALF IL-5 and IL-13 concentrations determined by LegendPlex. **d**, BAL eosinophil frequency and number after treatment. **e**, Lung histology. Representative images (left) and severity score (right). Data points in **c–e** represent individual mice (PBS, $n = 3$; IL-25, $n = 9$; IL-25 combined with NMU, $n = 7$). **f**, Airway resistance (Rrs) after graded methacholine (MeCh) challenge. Data points represent the mean of biological replicates (IL-25, $n = 7$; IL-25 combined with NMU, $n = 6$). **g, h**, ILC responses after HDM challenge. **g**, Frequency of ST2⁺ ILCs by flow cytometry. Data points are individual mice (wild-type (WT), $n = 15$; knockout (*Nmu* KO), $n = 13$). **h**, Frequency of ILCs expressing IL-5 or IL-13, by intracellular cytokine staining. Data points are individual mice ($n = 5$) in one of three individual experiments. Mean is indicated. Error bars, s.e.m.; * $P < 0.05$ by two-tailed t -test (**a, b, e, g, h**), one-way ANOVA (**c, d**), or two-way ANOVA (**f**); NS, not significant.

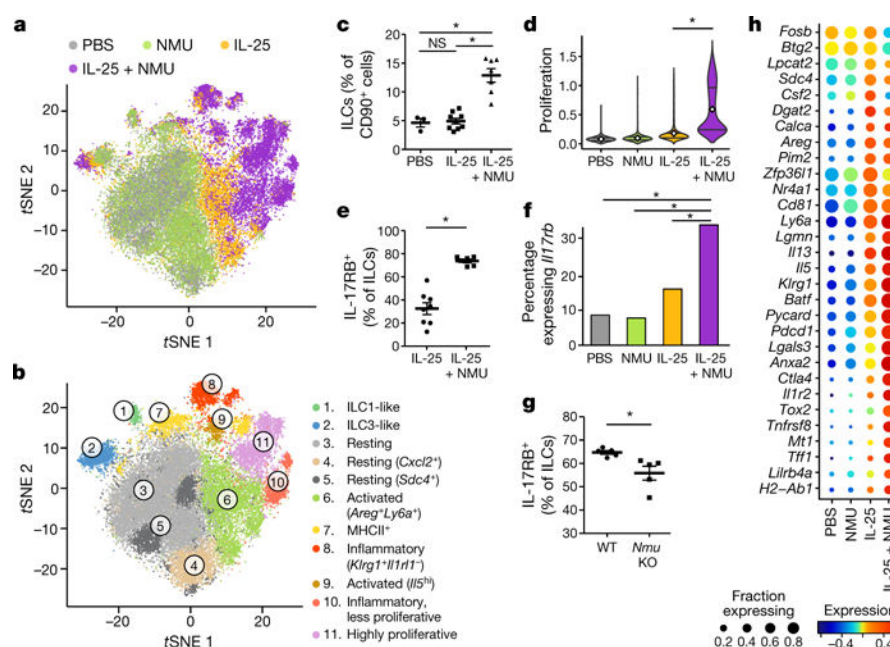


Figure 4. IL-25 and NMU synergize to activate inflammatory ILC2s

a, b, IL-25 combined with NMU induces distinct transcriptional states. tSNE plots of 35,542 ILCs from mice treated with the indicated stimuli, coloured by treatment (**a**) and cluster (**b**). **c**, ILC frequency determined by flow cytometry. **d**, Distribution of proliferation scores by treatment condition. Diamond indicates the mean; lines, first and third quartiles. **e–g**, IL-25 combined with NMU enhances IL-17RB expression on ILCs. **e**, IL-17RB⁺ ILC frequency by flow cytometry in one of two independent experiments. **f**, Frequency of *Il17rb*-expressing ILCs determined by scRNA-seq; * $P < 2.73 \times 10^{-10}$, logistic regression. **g**, IL-17RB⁺ ILC frequency after HDM challenge as determined by flow cytometry. **h**, Differentially expressed genes (y axis) by condition (x axis). Data points in **c**, **e**, **g** are individual mice (in **c**: PBS, $n = 3$; IL-25, $n = 9$; IL-25 combined with NMU, $n = 7$; in **e**: IL-25, $n = 8$; IL-25 combined with NMU, $n = 6$; in **g**: wild-type, $n = 5$; *Nmu*-knockout, $n = 5$). Mean is indicated. Error bars, s.e.m.; * $P < 0.05$ by one-way ANOVA (**c**) or two-tailed *t*-test (**d**, **e**, **g**).

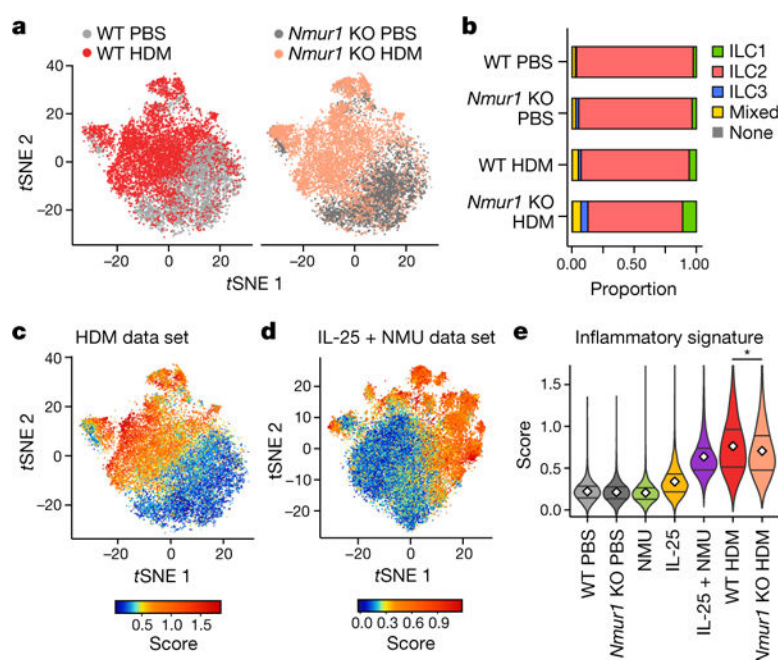


Figure 5. NMUR1-signalling regulates ILC responses after allergen challenge

a, HDM challenge induces distinct transcriptional states. ScRNA-seq profiles of 21,895 ILCs from wild-type (WT; left) and *Nmur1*-knockout (KO; right) on the same tSNE plot, coloured by treatment and genotype. **b**, Proportions of ILC subsets in each condition and genotype. **c–e**, An inflammatory ILC2 gene signature based on differential expression between ILCs from PBS- and HDM-treated mice. **c**, **d**, ILCs coloured by inflammatory ILC2 score, from HDM-challenged mice (**c**) and mice treated with PBS, NMU, IL-25 or IL-25 combined with NMU (**d**). **e**, Distribution of inflammatory ILC2 scores (y axis) in the indicated conditions. Diamond indicates the mean; lines, first and third quartiles; * $P < 4.9 \times 10^{-15}$, two-tailed *t*-test.